Please cite this article in press as: Cosi et al., Multiscale Modeling of Dyadic Structure-Function Relation in Ventricular Cardiac Myocytes, Biophysical Journal (2019), https://doi.org/10.1016/j.bpj.2019.09.023

Biophysical *Journal*
Article

Biophysical Society

Multiscale Modeling of Dyadic Structure-Function Relation in Ventricular Cardiac Myocytes

Filippo G. Cosi,[1,4,5] Wolfgang Giese,[2] Wilhelm Neubert,[2] Stefan Luther,[1,4,5] Nagaiah Chamakuri,[3] Ulrich Parlitz,[1,4,5] and Martin Falcke[2,6,7,*]

[1]Max Planck Institute for Dynamics and Self-Organization, Göttingen, Germany; [2]Max Delbrück Center for Molecular Medicine in the Helmholtz Association, Berlin, Germany; [3]Institute of Applied Mathematics, University of Hohenheim, Stuttgart, Germany; [4]Georg-August-Universität Göttingen, Institute for the Dynamics of Complex Systems, Göttingen, Germany; [5]DZHK (German Center for Cardiovascular Research), Partner Site Göttingen, Göttingen, Germany; [6]DZHK (German Center for Cardiovascular Research), Partner Site Berlin, Berlin, Germany; and [7]Department of Physics, Humboldt University Berlin, Germany

ABSTRACT Cardiovascular disease is often related to defects of subcellular components in cardiac myocytes, specifically in the dyadic cleft, which include changes in cleft geometry and channel placement. Modeling of these pathological changes requires both spatially resolved cleft as well as whole cell level descriptions. We use a multiscale model to create dyadic structure-function relationships to explore the impact of molecular changes on whole cell electrophysiology and calcium cycling. This multiscale model incorporates stochastic simulation of individual L-type calcium channels and ryanodine receptor channels, spatially detailed concentration dynamics in dyadic clefts, rabbit membrane potential dynamics, and a system of partial differential equations for myoplasmic and lumenal free Ca^{2+} and Ca^{2+}-binding molecules in the bulk of the cell. We found action potential duration, systolic, and diastolic [Ca^{2+}] to respond most sensitively to changes in L-type calcium channel current. The ryanodine receptor channel cluster structure inside dyadic clefts was found to affect all biomarkers investigated. The shape of clusters observed in experiments by Jayasinghe et al. and channel density within the cluster (characterized by mean occupancy) showed the strongest correlation to the effects on biomarkers.

SIGNIFICANCE Diseases such as myocardial infarction, aortic stenosis, tachycardia, hypertension, chronic ischemia, and atrial fibrillation have been related to changes inside the dyadic cleft, which is a subvolume of cardiac myocytes of $\sim 10^{-17}$ l (typical cell volume 10^{-11} l). However, exploration of the relation between subdyadic structures and disease is difficult because such microscopic structures in cells are in many cases not amenable to experimental manipulation, or experiments addressing them might not allow for simultaneous observation of cellular responses. Multiscale mathematical models can explore the relation between microscopic structures and cellular response. We show by mathematical modeling that the geometric properties of ryanodine receptor channel clusters within dyadic clefts affect cellular responses.

INTRODUCTION

The functioning of the heart is based on the precisely controlled contraction of its cardiac myocytes coordinated across the muscle by waves of membrane potential depolarizations (action potentials (APs)) emanating from the sinoatrial node. On the level of an individual cardiac myocyte, L-type Ca^{2+} channels (LCCs) open during an AP and trigger the release of Ca^{2+} from the sarcoplasmic reticulum (SR), which is the main intracellular Ca^{2+} storage compartment. The entailing global Ca^{2+} increase causes the binding of molecular motors to actin filaments in the sarcomeres and initiates contraction.

The SR forms a network of tubes that extend throughout the interior of the cell and can be divided into two main components known as junctional SR (jSR) and network SR (nSR). The cardiac myocyte is penetrated by a network of transverse tubules, which are plasma membrane invaginations that approach the jSR and thereby form small cellular subvolumes (see Fig. 1). These subvolumes, which have a height of 10–15 nm, are called dyadic clefts. Action potential gated LCC opening leads to calcium-induced calcium release (CICR) through ryanodine receptor channels (RyRs) in the jSR membrane. Ca^{2+} induces its own release because the opening probability of the RyRs increases with

Submitted May 31, 2019, and accepted for publication September 16, 2019.

*Correspondence: martin.falcke@mdc-berlin.de

Filippo G. Cosi and Wolfgang Giese contributed equally to this work.

Editor: Daniel Beard.

https://doi.org/10.1016/j.bpj.2019.09.023

Please cite this article in press as: Cosi et al., Multiscale Modeling of Dyadic Structure-Function Relation in Ventricular Cardiac Myocytes, Biophysical Journal (2019), https://doi.org/10.1016/j.bpj.2019.09.023

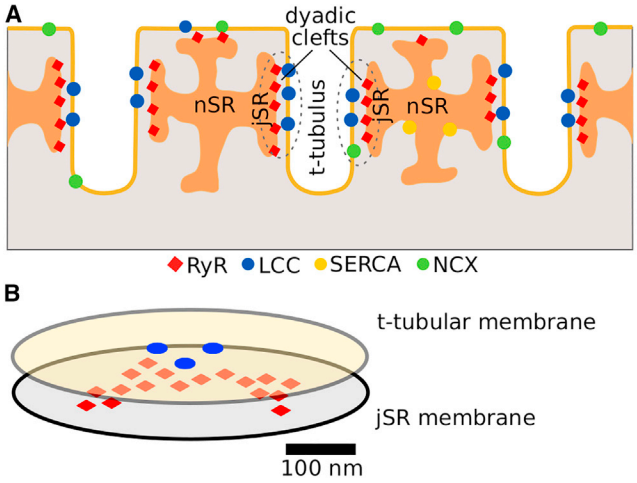

FIGURE 1 (*A*) Sketch of cellular level organization and transverse tubular structure in the cardiac myocyte. (*B*) Molecular level arrangement of LCCs and RyRs in a single dyadic cleft is shown. To see this figure in color, go online.

the local Ca^{2+} concentration at the channel. CICR is facilitated by the co-localization of LCCs in the transverse tubules membrane on the one side of a dyadic cleft and RyRs in the jSR membrane on the other side. The RyRs together with the LCCs and the associated jSR structure comprise the calcium release unit (CRU). Release from CRUs provides the Ca^{2+} triggering contraction of the sarcomeres. CRUs are concentrated in the structures connecting sarcomeres—the z-disks. The CRUs are arranged within z-disks with distances of less than 1 μm. The z-disks form a regular stack with a spacing of $\sim$2 μm.

CRUs behave stochastically because they contain a small number of ion channels. Because of CICR, they are excitable and can form sparks, which are the elementary events of Ca^{2+} release. Cooperation of several CRUs via CICR may generate unwanted Ca^{2+} waves. These processes occur on different time and length scales (see Fig. S1). The $[Ca^{2+}]$ changes inside the dyadic cleft happen within a few milliseconds; SR dynamics, on the other hand, act on a timescale of up to tens of seconds. We have spatial scales ranging from tens of nanometers in the dyadic cleft up to 100 μm in cell size. To account for these temporal and spatial scales, multiscale models with spatially distributed Ca^{2+} release sites have been developed (1–6). The model used here simulates the behavior of individual RyR and L-type calcium channels as well as the concentration gradients inside clefts. On cell level, we simulate the membrane potential and concentration dynamics. We do not use the approximation by spatial compartments for the bulk concentration dynamics but simulate the corresponding partial differential equations with the numerically required spatial resolution (1,6).

Common challenges with detailed multiscale modeling are the parameterization of the model by reproducing the values of a set of measured biomarkers (biomarkers are measurable properties of cells characterizing cell behavior) and the quantification of unknown values of parameters (7–10) because of the large number of simulations required for these purposes. Methods to quantify the relationship of variability and uncertainty of model inputs (parameter values) to outputs (simulated biomarker values), which are based on the construction of a response surface, have been recently suggested (7,8,11,12) and may spare many simulation runs. Exploiting the multiscale abilities of the model, we use biomarkers on different time and length scales for APs (seven biomarkers) and Ca^{2+} sparks (four biomarkers) to adapt our model to rabbit experimental results. Our systematic quantification of the relation between parameter and biomarker values uses an approximation by sums of polynomials (polynomial chaos expansion (12,13,14)). Sensitivity analysis identifies the parameters dominating the control of biomarker values—both in the mathematical sense of it and as the model's suggestion for most efficient control of the cell state (e.g., by post-translational modifications).

Diseases such as myocardial infarction, aortic stenosis, tachycardia, hypertension, and chronic ischemia are frequently related to changes in the dyadic cleft (15,16), which motivated several studies in recent years focusing on the details of the placement of RyR channels inside it. It turned out not to be on a square lattice as assumed before but to be less regular with respect to size and geometrical properties (16–24). The geometrical analysis revealed that channel positions in a cluster have random components and that cluster area is elongated in one direction rather than quadratic or circular (17–20,24,25). Although the cluster size heterogeneity has been related to spark probability (23), the functional consequences of the geometrical properties of RyR clusters are not so obvious yet. Modeling can investigate them only if intradyadic gradients are taken into account as our approach does and other studies on the CRU level did (22,25,26). We address the functional consequences of channel placement on CRU and cell level and compare them between the regular arrangement and configurations with increasing irregularity. To that end, we choose the rules of channel placement provided by Jayasinghe et al. (17) to generate cluster geometries and channel locations similar to experimental observation. We put CRUs with these cluster geometries into a ventricular cell model to study the relation between cluster structure and cell function.

MATERIALS AND METHODS

Mathematical model and methods

The mathematical model comprises whole cell dynamics as well as local molecular events (see Figs. 1 and S1). On the finest level, individual channels are represented as continuous time Markov chains, coupled by local gradients inside the dyadic space. Cell wide diffusion of $[Ca^{2+}]$ and its buffers is modeled by partial differential equations, which also include the fluxes generated by SR/endoplasmic reticulum Ca^{2+}-ATPase (SERCA), NCX (Na^{+}/Ca^{2+} exchanger), and the CRUs. Spatially averaged variables

Please cite this article in press as: Cosi et al., Multiscale Modeling of Dyadic Structure-Function Relation in Ventricular Cardiac Myocytes, Biophysical Journal (2019), https://doi.org/10.1016/j.bpj.2019.09.023

comprise membrane potential, [Na^+], and [K^+] which are generally assumed to not exhibit strong gradients on the subcellular level. A detailed description of the model can be found in (1,6) and Supporting Materials and Methods.

The finite element simulation toolbox DUNE has been used to solve the model equations (27,28). A complete description of the numerical approach is given in (1,6) and a short overview in Supplementary Materials and Methods.

Channel placement model

Mathematical models describing cellular calcium dynamics in cardiac myocytes generally omit a spatially resolved description of the single CRUs depicting them as point sources and/or neglect the internal structure of channel arrays inside dyadic clefts by assuming spatially homogeneous Ca^{2+} concentration (4,29–31). However, we take them into account as required by our investigation on RyR placement (1,6,32,33). To determine the RyR arrangement in the cleft, we use the placement algorithm suggested by Jayasinghe et al. (17), which provides channel locations closely resembling their experimental data. This placement algorithm determines channel locations as the sequence of positions in a two dimensional random walk with as many steps as channels in the dyad. The first RyR is placed in the center of the dyadic cleft. The position of the second RyR is found by a step in a random direction and with random length. The step length is drawn from a normal distribution (mean $\mu_{RyR} = 40.1$ nm, SD $\sigma_{RyR} = 7.4$ nm from (17)) with a cutoff accounting for the channel molecule diameter of 30 nm (34). The angle defining the direction is drawn from a uniform distribution in $[0,2\pi]$. Subsequent steps to channel positions obey the same rules plus the additional requirement to steer clear of existing channel molecules (excluded volume).

The first LCC channel is positioned at the center of the RyR cluster. In the following, LCCs are placed on a regular grid as in (1), again with a minimal distance of 30 nm from any other channel. Two examples of channel locations in a dyadic cleft generated this way are shown in Fig. 2 *C*.

Sensitivity analysis and construction of a response surface

We generated a population of models by varying five crucial model parameters using Latin hypercube sampling (35). The hypercube was formed by the axes in the parameter space representing k_{plus}, k_{close}, g_{RyR}, g_{LCC}, and $V_{P,max}$. All five parameters were varied by a factor of 10 (see Table 1). The choice of the parameter ranges was based on values in the literature (1,36,37). The literature values may depart slightly from the chosen ranges because of different pacing cycle lengths. The pacing cycle length used in our simulations is 350 ms. The model simulations have identical initial conditions except for the stochasticity of the geometric channel arrangement and selected model parameters. All samples were run for the same simulation time. The resulting set of simulation results was analyzed by Bayesian linear regression (38) and polynomial chaos expansion (13) to obtain local and global parameter dependencies.

Bayesian linear regression was used to obtain an estimate of local parameter sensitivity coefficients. The model sensitivity s_{XY} from the linear fit was computed from the following:

$$s_{XY} = \frac{X_{\text{ref}}}{Y_{\text{ref}}} S_{XY}, \tag{1}$$

where S_{XY} is the slope (along parameter X) from multiple linear regression in a specified neighborhood of a reference parameter set (marked in Figs. 5 and 7 as a red cross). Here X_{ref} denotes the corresponding parameter value, and Y_{ref} is the corresponding reference value of the biomarker. We can read off the local strength, direction, and uncertainty of output change with respect to the variation of a selected parameter from these sensitivity coefficients. Because the mathematical model is stochastic, the output cannot be predicted with absolute certainty but with some probability only. We therefore used Bayesian linear regression to obtain a proper quantification of the uncertainty in the predictions. The algorithms were implemented using the Python library Edward (39) and TensorFlow (40) toolboxes. Although these sensitivities are based on a linear regression, we complemented our investigations by calculating Sobol coefficients (see Fig. S3), which serve as a measure of global sensitivities for nonlinear models (41).

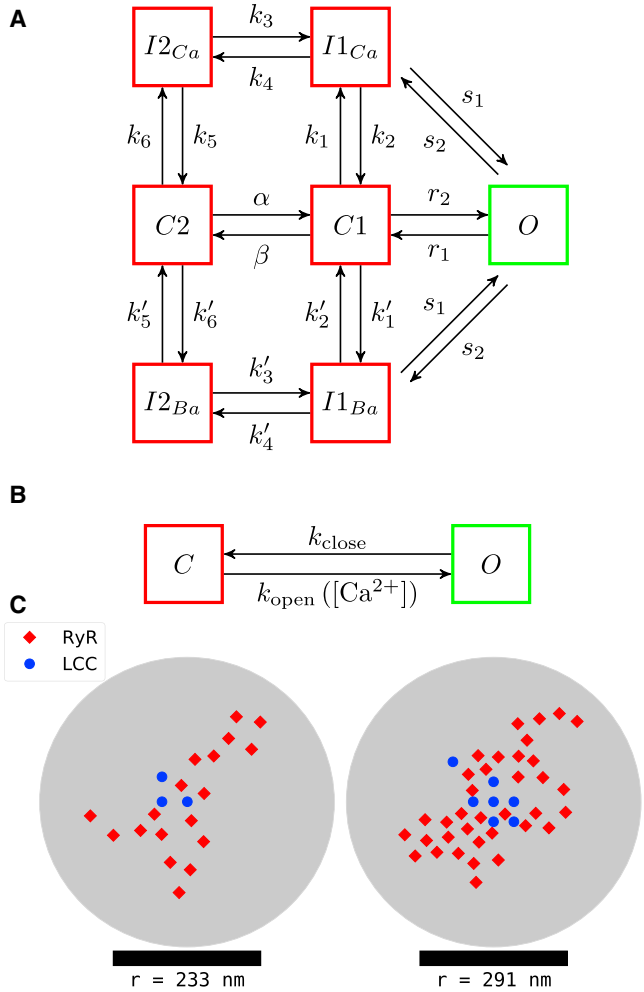

FIGURE 2 (*A*) L-type Ca^{2+} channel (LCC) state scheme with the open state marked in green (36). (*B*) Ryanodine receptor (RyR) state scheme with the open state marked in green (26); the open rate k_{open} depends on dyadic as well as on jSR [Ca^{2+}] as described in more detail in Supporting Materials and Methods. (*C*) Shown are two examples of placements of LCCs (*blue circles*) and RyRs (*red diamonds*) in single dyadic clefts with radii *r*. To see this figure in color, go online.

To quantify the effect parameters have on the biomarkers, we used an approximation method known as polynomial chaos expansion. For the polynomial chaos expansion, an orthonormal basis of polynomials was generated by using a Python-specific library called Chaospy (42). We assumed uniform distribution of the input parameters and therefore used Legendre polynomials for the regression fit. Using a polynomial degree p and a number of parameters d, the number of polynomial coefficients, which have to be determined, can be calculated from:

$$n = \binom{d+p}{d}. \tag{2}$$

Please cite this article in press as: Cosi et al., Multiscale Modeling of Dyadic Structure-Function Relation in Ventricular Cardiac Myocytes, Biophysical Journal (2019), https://doi.org/10.1016/j.bpj.2019.09.023

TABLE 1 Parameters, Sampling Ranges, and Suggested Parameter Set for Spark and Action Potential Simulations

Parameter	Description	Sampling Range	Suggested Value	Accepted Range
k_{plus} [ms^{-1} $\mu M^{-\eta}$]	RyR opening rate	5.0×10^{-5}–5.0×10^{-4}	1.5×10^{-4}	$(1.1–2.3) \times 10^{-4}$
k_{close} [ms^{-1}]	RyR closing rate	0.1–1.0	0.5	0.28–0.55
g_{RyR} [μm^3 s^{-1}]	RyR Ca^{2+} permeability	3.0×10^{-4}–3.0×10^{-3}	7.5×10^{-4}	$(5.9–8.4) \times 10^{-4}$
g_{LCC} [μm^3 s^{-1}]	LCC Ca^{2+} permeability	4.5×10^{-4}–4.5×10^{-3}	3.2×10^{-3}	$(1.7–3.4) \times 10^{-3}$
$V_{P,max}$ [μM ms^{-1}]	maximal SERCA uptake rate	0.15–1.5	0.55	0.08–0.71

The output stays in the literature range of all biomarker values, if the corresponding parameter is varied within the range given in the fifth column (accepted range), whereas other parameter values are kept at the value in the fourth column (suggested value).

The required number of data points usually exceeds the number of coefficients by at least a factor of 2–3 to prevent overfitting (43). To obtain an optimal regression and polynomial degree, we quantified the commonly used least-squares fit error and the cross-validation error as explained in Supporting Materials and Methods.

RESULTS

The simulated time course of the Ca^{2+} concentration inside a dyadic cleft during an AP is illustrated in Fig. 3 and Video S1. Gradients comprise three orders of magnitude (0.1–150 μM) upon the opening of the first channel. The concentration outside the cleft space changes quickly, such that we observe gradients from ~150 μM at the boundary of the cleft to ~300 μM at open channels later during the event. Hence, the opening rate of RyRs close to open channels is initially six orders of magnitude and, later into the spark, is ~4 times faster than the rate of channels further away (see Eq. S11; Table S2). The simulations illustrate the strong impact of gradients on the transition from one open LCC (or RyR, quark) to a spark and the quantitative effect on the calcium transient. This applies throughout an AP, as Video S1 shows.

The jSR concentration decreases rapidly upon the onset of release (Fig. 3). In case of sparks, this helps terminating release due to decreasing release current and consequently less coupling of RyRs by CICR. This mechanism is in agreement with earlier studies (25,26,44). In case of AP simulations, the jSR concentration continues to decrease on average till about the end of the membrane potential plateau (Fig. 3).

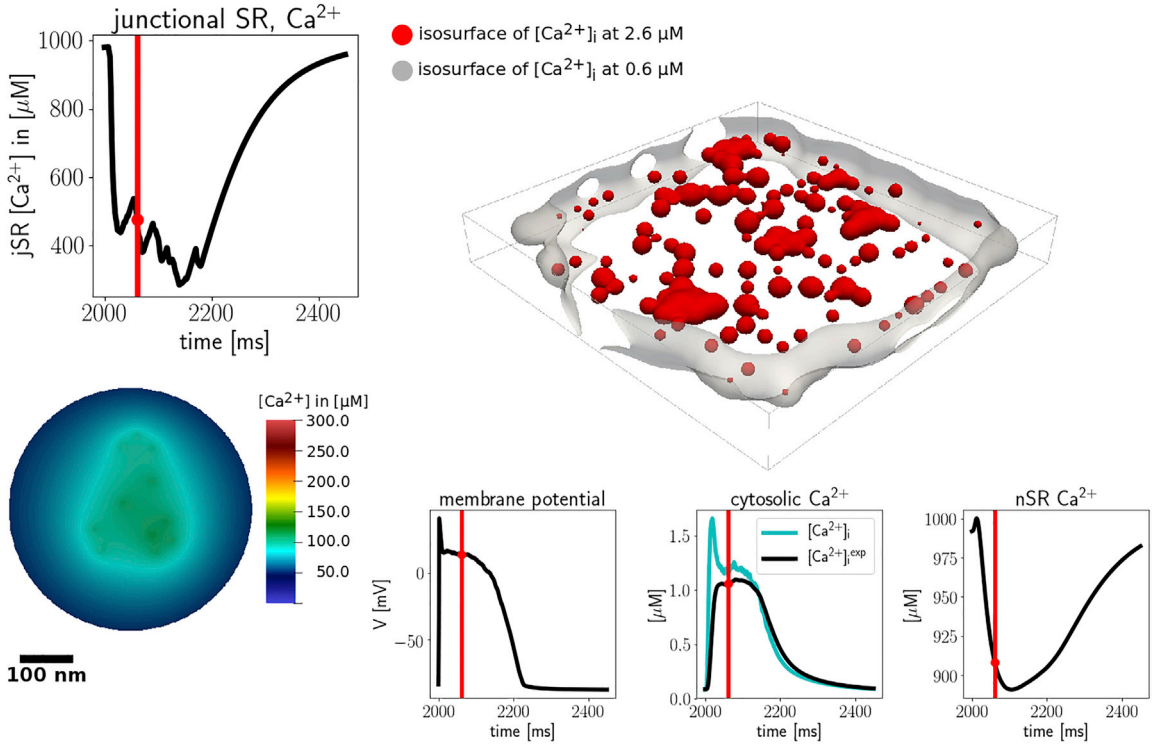

FIGURE 3 Multiscale simulation. Shown is a snapshot of the concentration profile in a dyadic cleft and the jSR concentration time course of this CRU. A snapshot of isoconcentration surfaces (0.6 μM, 2.6 μM) of the cytosolic concentration $[Ca^{2+}]_i$ of the whole z-disk (15 μm × 15 μm × 2 μm) with 320 dyadic clefts and the time course of the membrane potential, average $[Ca^{2+}]_i$, and average nSR $[Ca^{2+}]$ are shown on the right-hand side. The red line indicates the time point at which the snapshots were captured. A corresponding simulation for one AP is shown in Video S1. To see this figure in color, go online.

Please cite this article in press as: Cosi et al., Multiscale Modeling of Dyadic Structure-Function Relation in Ventricular Cardiac Myocytes, Biophysical Journal (2019), https://doi.org/10.1016/j.bpj.2019.09.023

Fig. 3 also shows the cytosolic concentration $[Ca^{2+}]_i$ caused by the release from all CRUs in the z-disk (15 μm $\times$ 15 μm $\times$ 2 μm) and the membrane potential, average $[Ca^{2+}]_i$, and average nSR concentration. The variable size of the volumes enclosed by the 2.6 μM isoconcentration surface illustrates the randomness and heterogeneity of release events. Refined numerical grids around CRUs guarantee the faithful simulation of Ca^{2+} and buffer diffusion between them (6). In that way, we can simulate the concentration dynamics from subdyadic to cellular length and timescales.

To facilitate the comparison of experimentally measured and simulated $[Ca^{2+}]$, we simulated a fluorescent buffer (see Fig. S4). This allowed us to emulate the approximation of $[Ca^{2+}]_i$ as it would be measured by a single wavelength Fluo-4 experimental recording using an in vitro calibration approach as described in (45):

$$\left[Ca^{2+}\right]_i^{exp} = K_d \frac{F - F_{min}}{F_{max} - F}, \quad (3)$$

where K_d is the dissociation constant of Fluo-4, F is the experimentally measured fluorescence intensity (the spatial average of b_f), F_{max} is the measured fluorescence intensity in Ca^{2+}-saturated dye (here, this is set as b_f^{tot}), and F_{min} is the measured fluorescence intensity in the absence of Ca^{2+} (here, set to zero).

Quantification of parameter values based on biomarkers

A population of simulated cells was generated as described in Materials and Methods. We identified valid parameter sets by filtering all simulation results for those providing biomarker values in the ranges stated in literature (see Tables 2 and 3). The biomarker resting membrane potential, maximum membrane potential, dome membrane potential, and $[Na^+]_i$ (see Table 2) are mainly determined and met by the Mahajan electrophysiology model we use and have essentially not been affected by the parameter variations considered here (36). Results of AP simulations were filtered by taking the biomarkers APD90, peak systolic $[Ca^{2+}]$, and mean diastolic $[Ca^{2+}]$ into account. The spark biomarkers used in the filtering of the spark simulations are the spark rate (i.e., events with at least two simultaneously open RyRs in the same cleft), the average FDHM, the mean of the Ca^{2+} peak value of sparks, and the ratio between quarks and sparks. Quarks are events in which exactly one RyR opens in a given cleft. The overlap of both filtering results led to the suggested parameter value set in Table 1. We performed 281 simulations for APs. Of those, 23 parameter sets passed the biomarker ranges stated above. Out of the 297 Ca^{2+} spark simulations, 20 simulations passed the ranges for the Ca^{2+} sparks. The suggested value (Table 1, fourth column) fulfills the requirement for all seven biomarkers.

TABLE 2 Biomarkers Ranges for Action Potentials

Biomarker	Range	Description
Max V_m	46 $\pm$ 4.5 mV	maximal value of AP peaks
Resting V_m	−77.4 $\pm$ 3.9 mV	resting value of the AP
Dome V_m	15.2 $\pm$ 10.1 mV	peak in the plateau phase
APD90	150–200 ms	APD at 90%
Systolic $[Ca^{2+}]$	0.6–1.2 μM	peak systolic calcium
Diastolic $[Ca^{2+}]$	0.1–0.25 μM	diastolic calcium
$[Na^+]_i$	10.5–11.5 mM	intracellular sodium

Table S1 also lists references.

TABLE 3 Biomarker Ranges for Ca^{2+} Sparks

Biomarker	Range	Description
FDHM	8.0–17.5 ms	FDHM
Spark rate	1–5 $\mu m^{-1}s^{-1}$	number of sparks per μm cell and second
Quark to spark ratio	0.2–1.1	number of quarks/number of sparks
Peak $[Ca^{2+}]$	10.0–22.0 μM	average maximal $[Ca^{2+}]$
Peak $[Ca^{2+}]_i^{exp}$	0.6–1.2 μM	during a spark

Table S1 also lists references.

Sensitivity analysis and response surfaces of AP biomarkers

Sensitivity analysis provides information on how changes of input parameters affect a particular biomarker value. We have chosen to vary the five parameters k_{plus}, k_{close}, g_{RyR}, g_{LCC}, and $V_{P,max}$ in this analysis. All of them are related to Ca^{2+} as the focus of this study. The parameters setting the RyR open probability (k_{plus}, k_{close}) and SERCA uptake ($V_{P,max}$) were chosen because they are targets of drugs or post-translational modifications. We vary the RyR conductivity g_{RyR} because the in vivo single channel current is not well known. The LCC conductivity g_{LCC} turned out to be an important parameter in preliminary simulations.

We have chosen the suggested values of the parameters in Table 1 as reference for all sensitivities in this study. Fig. 4 shows the sensitivities for the AP biomarkers (APD90, peak systolic $[Ca^{2+}]$, and mean diastolic $[Ca^{2+}]$) versus the varied parameters. The LCC permeability g_{LCC} has the strongest positive impact on all three biomarkers (Fig. 4). The positive correlation of APD90 with g_{LCC} we observe is in line with results by Britton et al. (46). AP durations (APDs) are positively influenced by the RyR opening rate k_{plus} and negatively by their closing rate k_{close}, whereas for the systolic $[Ca^{2+}]_i$ peak and diastolic $[Ca^{2+}]_i$, the opposite is true. The influence of the opening and closing rates of the RyRs on the APD mediates the effect these two parameters have on the $[Ca^{2+}]_i$ values. An increase of k_{plus} decreases $[Ca^{2+}]_i$ because it prolongs the AP. This entails longer Ca^{2+} release, which, in the end, reduces SR $[Ca^{2+}]$ and the release and leak currents. We see the opposite effect when increasing k_{close}. It

Please cite this article in press as: Cosi et al., Multiscale Modeling of Dyadic Structure-Function Relation in Ventricular Cardiac Myocytes, Biophysical Journal (2019), https://doi.org/10.1016/j.bpj.2019.09.023

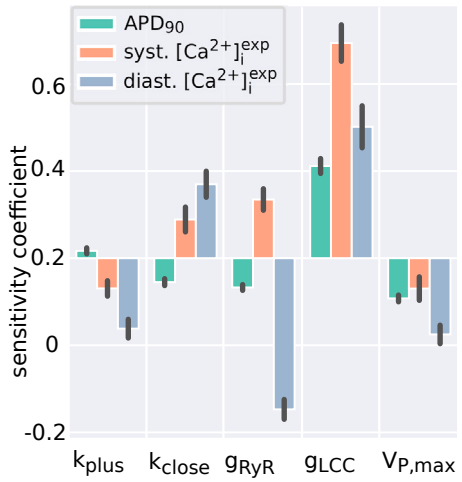

FIGURE 4 Sensitivity values for APD90, systolic $[Ca^{2+}]_i^{exp}$, and diastolic $[Ca^{2+}]_i^{exp}$. Black bars represent the SD for the sensitivity coefficients obtained from Bayesian inference and indicate the uncertainty in the estimates. To see this figure in color, go online.

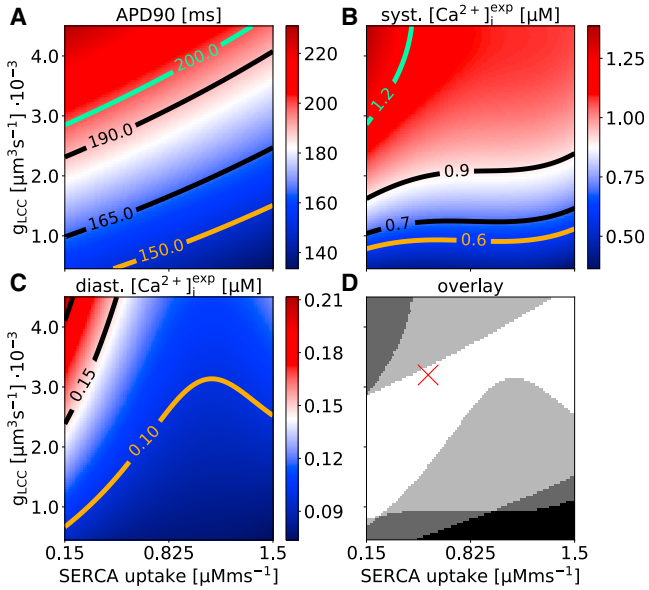

FIGURE 5 (*A–C*) Contour plots for the mean values of APD90, peak systolic $[Ca^{2+}]_i^{exp}$, and mean diastolic $[Ca^{2+}]_i^{exp}$ in dependence on LCC permeability g_{LCC} and maximal SERCA uptake $V_{P,max}$ with the values for k_{plus}, k_{close}, and g_{RyR} fixed to the values in Table 1 (fourth column). The iso lines for the upper and lower parameter values of the literature ranges are color coded in green and orange, respectively. (*D*) Shown are the contours limiting the literature value ranges for all three biomarkers in a single plot. The white area outlines the parameter region for g_{LCC} and $V_{P,max}$ within which all three AP biomarkers are within the literature ranges. The red mark indicates the parameter set listed in Table 1 (fourth column), meeting also the spark biomarker requirements. To see this figure in color, go online.

shortens the AP and increases SR $[Ca^{2+}]$ and hence also the release and leak current.

Extraction of more detailed information is based on the response surfaces. They provide an approximation for the dependency of each biomarker on the varied parameters. We use them to draw contour plots for biomarker values in dependency on parameter values (Fig. 5). The values of the parameters not varied in these plots are listed in Table 1 (fourth column) and Tables S2–S9.

The strong influence of g_{LCC} on the AP biomarkers motivates the focus mainly on this parameter and how its change might be compensated for by a change of another parameter. Fig. 5 depicts biomarker values computed in the g_{LCC}-$V_{P,max}$ plane. The iso lines for the upper and lower parameter values of the literature ranges are color coded in green and orange, respectively. From Fig. 5, we can read off how coordinated parameter changes can maintain important biomarkers as, for instance, APD90. Interestingly, the contours of iso-APD90 and isosystolic $[Ca^{2+}]$ are similar, and a coordinated change of SERCA uptake and LCC current along them could maintain approximately both but would affect mean diastolic $[Ca^{2+}]$.

Sensitivity analysis and response surfaces of spark biomarkers

Fig. 6 shows the sensitivities of the spark biomarkers with respect to the varied parameters. The spark rate is mainly influenced by the opening probability of the RyR k_{plus} and the RyR permeability g_{RyR}. Surprisingly, the full duration at half maximum (FDHM) is only weakly affected by all five parameters. Peak calcium strongly responds to changes of the RyR permeability. The quark to spark ratio is strongly negatively affected by changes in k_{plus} and g_{RyR} and positively by k_{close}.

The response surfaces of FDHM, spark rate, and $[Ca^{2+}]_i^{exp}$ are depicted in Fig. 7. $[Ca^{2+}]_i^{exp}$ was calculated from Ca^{2+}-bound dye buffer, as in experimental analyses, by using Eq. 3. Although this inferred $[Ca^{2+}]$ has a reasonable accuracy for the mean $[Ca^{2+}]$ during APs (see Fig. 3), our simulations suggest that it fails for the quantification of spark peak $[Ca^{2+}]_i$ (compare Figs. S4 and S7). Whereas the true peak $[Ca^{2+}]_i$ reaches values of more than 20 μM for single sparks, the inferred experimental concentration $[Ca^{2+}]_i^{exp}$ only reaches values slightly above 1 μM. A similar discrepancy occurs for the spark FDHM. Although the true underlying spark events appear to be short release events with a duration of 5–15 ms, the FDHM for the inferred $[Ca^{2+}]_i^{exp}$ is by factor of $\sim$2 longer.

Functional consequences of geometrical properties of RyR clusters

We start with comparing two different models for RyR placement in clusters. The first model assumes a regular arrangement with equidistant spacing (40 nm) of RyRs on a regular grid, whereas the second one assumes irregular clustering properties on the basis of the measurements of

Please cite this article in press as: Cosi et al., Multiscale Modeling of Dyadic Structure-Function Relation in Ventricular Cardiac Myocytes, Biophysical Journal (2019), https://doi.org/10.1016/j.bpj.2019.09.023

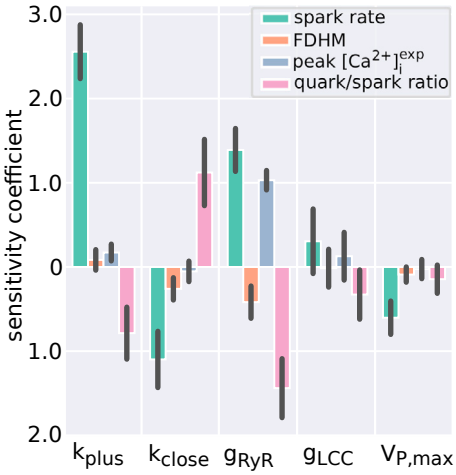

FIGURE 6 Sensitivity values for spark rate, mean peak $[Ca^{2+}]$, spark FDHM, and quark to spark ratio. Black bars represent the SD for the sensitivity coefficients obtained from Bayesian inference and indicate the uncertainty in the estimates. To see this figure in color, go online.

Jayasinghe et al. (17) as described before. We use the suggested values of the parameter set in Table 1 and performed 10 simulations for each placement model. Channel numbers for the individual CRUs are drawn from the same distribution (Eq. S12) for both groups. Differences between the individual simulations even within one placement model group arise from the randomness of channel numbers in CRUs and their placement. We find clear differences of biomarker values between the two placement models (Figs. 8 and 9). Hence, the dyadic substructure clearly affects cellular responses.

Geometric effects within the placement model by Jayasinghe et al. are shown in Fig. 10. A variety of channel configurations has been generated by sampling from the placement model distributions and additionally varying the distribution parameters. Although channel configurations have been characterized successfully by the adjacency matrix (22,26), we are looking here for a simpler approach. We characterized channel configurations by a variety of measures (average nearest- and four nearest-neighbor distance, area per channel determined by convex hull, and mean occupancy (see Fig. S5)) and found mean occupancy to show the strongest correlation with biomarker values. Mean occupancy is 1 if all RyRs are far apart and 0 if all RyRs are in the same spot (Fig. S5).

APD90, peak systolic $[Ca^{2+}]_i^{exp}$, and diastolic $[Ca^{2+}]_i^{exp}$ decrease with increasing mean occupancy (Fig. 10). This concerted decrease reflects the correlation between these values found in the contour plots in Fig. 5, too. All three trends are in line with the general picture of decreased Ca^{2+} release due to increased mean occupancy. Hence, we find effects of dyadic substructure also within one placement concept.

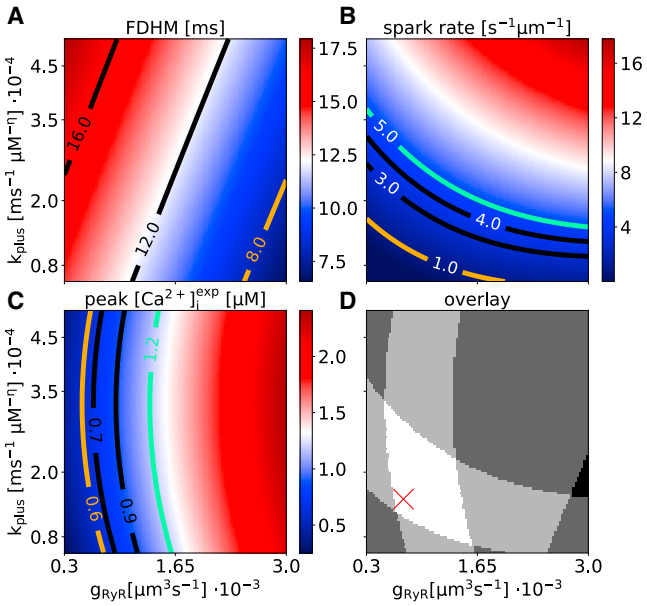

FIGURE 7 (*A–C*) Contour plots for the mean values of FDHM, spark rate, and peak $[Ca^{2+}]_i^{exp}$ inferred from Fluo-4 bound Ca^{2+} (Eq. 3) in dependence on the RyR permeability g_{RyR} and opening rate k_{plus} with the values for g_{LCC}, k_{close}, and $V_{P,max}$ fixed to Table 1 (fourth column). The iso lines for the upper and lower parameter values of the literature ranges are color coded in green and orange, respectively. (*D*) Shown are the contours limiting the literature value ranges for all three biomarkers in a single plot. The white area outlines the parameter region for g_{RyR} and k_{plus} within which all three spark biomarkers are within the literature ranges. The red mark indicates the parameter set listed in Table 1 (fourth column), meeting also the AP biomarker requirements. To see this figure in color, go online.

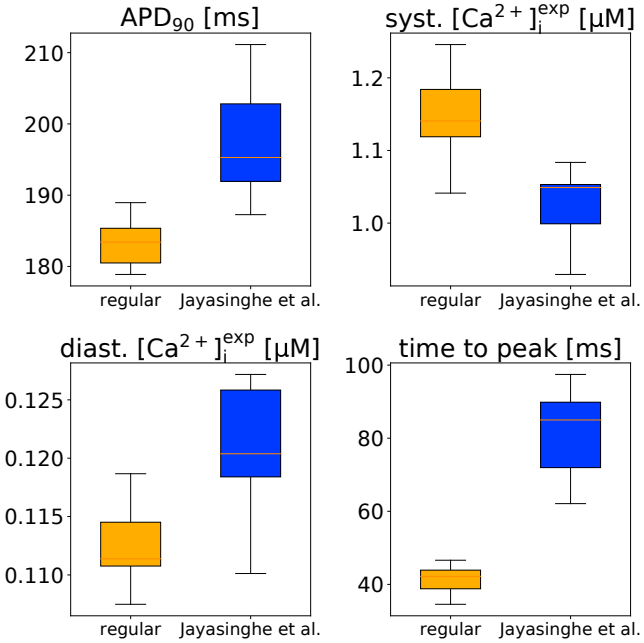

FIGURE 8 AP biomarker values APD90, systolic and diastolic $[Ca^{2+}]_i^{exp}$, and time to peak from simulations with two different RyR placement models, which are explained in the text. The boxplots are standard box and whisker diagrams. To see this figure in color, go online.

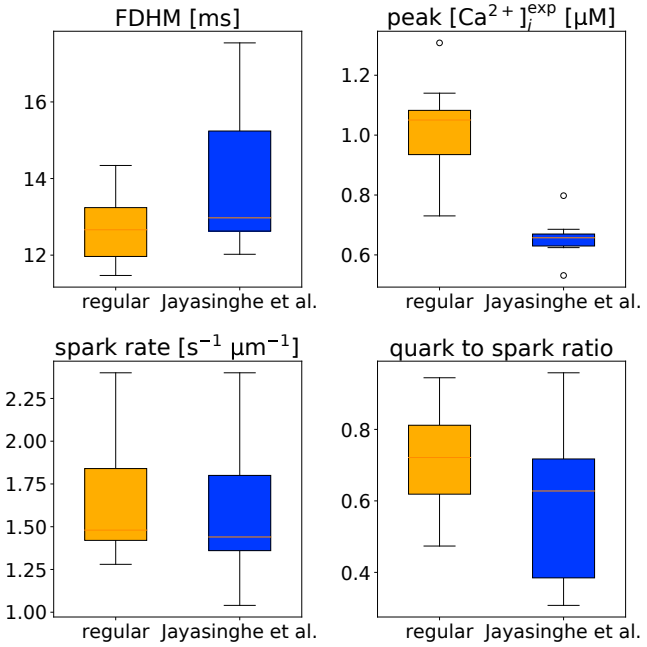

FIGURE 9 Spark biomarker values FDHM, peak $[Ca^{2+}]_i^{exp}$, spark rate, and quark to spark ratio from simulations with two different RyR placement models. The boxplots are standard box and whisker diagrams. To see this figure in color, go online.

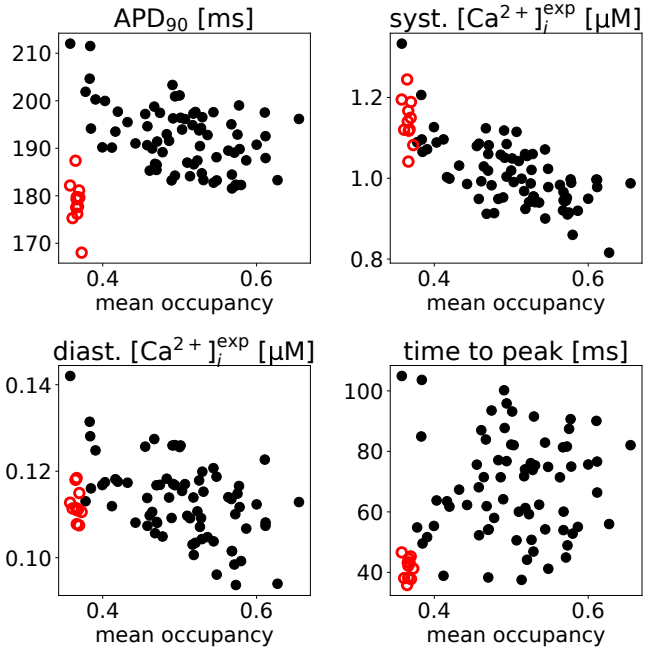

FIGURE 10 The relation between mean occupancy, as described in Fig. S5 and averaged over all CRUs, and the biomarkers APD90, systolic and diastolic $[Ca^{2+}]_i^{exp}$, and time to peak. Each dot corresponds to one simulation. Black dots mark Jayasinghe placement, and red circles mark regular placement. The Jayasinghe placement with the measured parameters has a mean occupancy of ∼0.49. The slopes of a linear regression for the Jayasinghe placement are as follows: APD90 −38 ms, systolic $[Ca^{2+}]_i^{exp}$ −0.68 μM, diastolic $[Ca^{2+}]_i^{exp}$ −0.056 μM, and time to peak 13 ms. To see this figure in color, go online.

The regular placement exhibits smaller APD90, larger peak systolic $[Ca^{2+}]_i^{exp}$, and shorter time to peak (Fig. 10). We assume that this is caused by the relation between LCC placement and the overall cluster shape. LCC locations were chosen according to the same rules described above for both placement methods. The Jayasinghe placement produces elongated clusters, and the regular placement produces quadratic clusters. Hence, the average RyR distance to the closest LCC is smaller with the regular placement than with the Jayasinghe placement, which entails stronger LCC-RyR coupling. This stronger and earlier Ca^{2+} release causes faster Ca^{2+}-dependent inhibition of LCCs and thus shorter APD.

The strength of the coupling of RyRs by Ca^{2+} diffusion decreases with increasing mean occupancy. The averages of spark biomarker values depend in the expected manner on occupancy as the slopes of the linear regressions show (Fig. 11). FDHM increases with increasing mean occupancy, reflecting the known phenomenon of slower termination of sparks with weaker spatial coupling of RyRs. Correspondingly, peak systolic $[Ca^{2+}]_i^{exp}$ and spark rate decreases with increasing mean occupancy. Large quark to spark ratios were found with weaker RyR coupling at large mean occupancy only. The spark biomarker values exhibit much stronger fluctuations than the AP simulations. The results with regular placement fit into the relation on mean occupancy.

Only the specific realizations of channel numbers in the individual CRUs vary between the individual simulations with the regular placement. Simulations with the Jayasinghe placement are distinguished by both channel number realizations and specific placement. Hence, comparing the scatter of the biomarker value results with regular placement (red circles) with the Jayasinghe placement (black dots) in Figs. 10 and 11 provides an idea of how much of the variability is due to the randomness of channel numbers per CRU. The variability due to channel number randomness is comparable to the total variability for the spark biomarkers FDHM and rate (Fig. 11). Jayasinghe placement increases the quark to spark ratio variability with increasing mean occupancy because coupling between channels becomes weaker. Surprisingly, the regular placement has a larger variability of the peak $[Ca^{2+}]_i^{exp}$ than the Jayasinghe placement because it exhibits also very large values. The same comparison for the AP simulations suggests variability of peak systolic $[Ca^{2+}]_i^{exp}$ to result mainly from channel number variability. Variability of APD90, diastolic $[Ca^{2+}]_i^{exp}$, and time to peak increase substantially because of the Jayasinghe placement.

DISCUSSION

Parameterization of detailed multiscale models faces the problem of large computational costs required for

Please cite this article in press as: Cosi et al., Multiscale Modeling of Dyadic Structure-Function Relation in Ventricular Cardiac Myocytes, Biophysical Journal (2019), https://doi.org/10.1016/j.bpj.2019.09.023

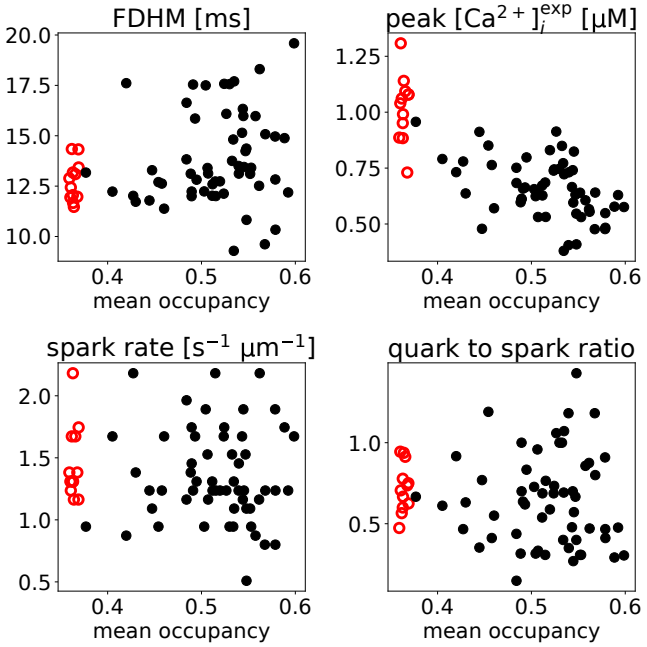

FIGURE 11 The relation between mean occupancy, as described in Fig. S5 and averaged over all CRUs, and the biomarkers FDHM, peak $[Ca^{2+}]_i^{exp}$, spark rate, and quark to spark ratio. Each dot corresponds to one simulation. Black dots mark Jayasinghe placement, and red circles mark regular placement. The Jayasinghe placement with the measured parameters has a mean occupancy of ~0.49. The slopes of a linear regression for the Jayasinghe placement are as follows: FDHM 7.42 ms, peak $[Ca^{2+}]_i^{exp}$ −0.88 μM, spark rate −0.37 s^{-1}, and quark to spark ratio −0.11. To see this figure in color, go online.

simulations, which often prevents systematic parameter searches. These models require large efforts to reduce compute time and methods concluding parameter dependencies from a minimum of simulations. We reported our efforts to speed up simulations in previous studies (1,6). Here, we present a parameterization of the model to experimental data. To that end, we identified ranges of altogether 11 biomarker values from literature, four of them were fulfilled by model output, mainly based on previous work by Mahajan et al. (36), and seven of them were affected by our spatially detailed approach and had to be met by our parameterization procedure. The multiscale set up of our model allowed for detailed channel placement inside dyadic clefts, according to measurements in Jayasinghe et al. (17). Accordingly, we focused here on parameters that are crucial for the Ca^{2+} handling in the microscopic domain of the dyadic cleft: the opening and closing rates of RyRs k_{plus} and k_{close}, the RyR permeability g_{RyR}, the LCC permeability g_{LCC}, and the strength of SERCA uptake $V_{P,max}$.

In the case of AP simulations, LCC permeability g_{LCC} variation has the strongest impact on cell behavior, as illustrated by the sensitivities in Fig. 4. The response surfaces in Fig. 5 illustrate the strong correlation between APD and the systolic $[Ca^{2+}]_i$ values. As an example of a control strategy suggested by response surfaces, we note that a coordinated change of g_{LCC} and $V_{P,max}$ can approximately maintain APD and systolic $[Ca^{2+}]_i$ while lowering diastolic $[Ca^{2+}]_i$, if the initial APD is in the lower range of the literature values. That would be a strategy to decrease the propensity for diastolic triggered events while maintaining contraction.

The spark simulations show that k_{plus}, k_{close}, and g_{RyR} affect the spark rate in the way we expected: k_{plus} and g_{RyR} positively, k_{close} negatively. Their effect on the quark to spark ratio can be comprehended by considering the probability that the first open RyR does open another one, thus turning a quark into a spark. That probability increases with k_{plus} and g_{RyR} and therefore reduces the quark to spark ratio and vice versa with k_{close}. The weak effect of all five parameters on the FDHM is surprising at a first glance; however, it agrees with the results by Cannell et al. (25) for the latency of induction decay.

The Jayasinghe placement affects the mean and SD of the AP biomarker values and mean and/or the SD of the spark biomarker values we have investigated. Hence, subdyadic structure matters. Figs. 8, 9, 10, and 11 report the effect of the Jayasinghe placement compared to the regular placement. These effects are due to cluster shape and channel density. The elongated shape of the clusters generated by the Jayasinghe placement weakens LCC-RyR coupling (compared to the regular placement), which increases time to peak and APD90 and affects indirectly diastolic and peak systolic $[Ca^{2+}]_i^{exp}$. Mean occupancy is related to density and mean channel distance. In principle, the SD of channel distances could also have an effect on CRU dynamics by generating highly coupled subclusters at large SD. However, that is not supported by our simulations.

We found the effects of channel placement, which might be affected by specifics of our cleft model. We assume a fraction of 50% of total Ca^{2+} to be buffered by mobile buffers based on estimates from (26). This estimate assumes ATP ($K_D \approx 200$ μM (26)) to be the dominating mobile buffer at Ca^{2+} concentrations occurring in the dyadic space. ATP levels may change to a degree affecting dyadic buffering in pathological states; however, this was not in the scope of this study (47,48). We use an effective diffusion coefficient of 100 μm^2 s^{-1} inside the cleft as well as a quasistatic approximation for the concentration profiles (see Supporting Materials and Methods; (1,6,32,33)). Coupling of RyRs upon the opening of a channel with dynamic concentration profiles is initially weaker than with quasistatic profiles. Geometric effects are more important with weak spatial coupling. Hence, we assume that dynamic profiles would slightly amplify them. The timescales of the cytosolic concentration around the cleft space dominate the dynamics upon closing. They are captured by our model. The diffusion coefficient in the dyadic space has not been measured, and we informed our model on the basis of other modeling studies (25,26,49). Because we are using an effective value, it is rather at the upper end of the currently accepted range.

Please cite this article in press as: Cosi et al., Multiscale Modeling of Dyadic Structure-Function Relation in Ventricular Cardiac Myocytes, Biophysical Journal (2019), https://doi.org/10.1016/j.bpj.2019.09.023

In summary, we may rather underestimate than overestimate the geometrical effects.

In this study, we used multiscale modeling in two ways complementary to experimental studies. We observed local dynamics and cellular behavior simultaneously, and we modified subdyadic structures, which cannot be modified by experimental means. That provided insight into structure-function relations across multiple scales. Our results suggest that both the mean occupancy and the overall cluster shape affect APs and cytosolic Ca^{2+} transients.

SUPPORTING MATERIAL

Supporting Material can be found online at https://doi.org/10.1016/j.bpj.2019.09.023.

AUTHOR CONTRIBUTIONS

M.F., W.G., F.G.C., N.C., U.P., and S.L. designed the research. W.G., F.G.C., and W.N. performed the research. W.G. and F.G.C. analyzed the data. M.F., F.G.C., W.G., N.C., U.P., and S.L. wrote the manuscript.

ACKNOWLEDGMENTS

N.C. acknowledges support from the Science and Engineering Research Board, Department of Science and Technology, India (EMR/2017/000664 and MTR/2017/00 0598). F.G.C., U.P. and S.L. acknowledge support from the German Research Foundation (DFG) via SFB 937 (project A18). S.L. acknowledges support through the German Center for Cardiovascular Research, partner site Göttingen. F.G.C. acknowledges support by the Physics to Medicine program and the Göttingen Graduate Center for Neurosciences, Biophysics, and Molecular Biosciences.

REFERENCES

1. Vierheller, J., W. Neubert, …, N. Chamakuri. 2015. A multiscale computational model of spatially resolved calcium cycling in cardiac myocytes: from detailed cleft dynamics to the whole cell concentration profiles. *Front. Physiol.* 6:255.
2. Rajagopal, V., G. Bass, …, C. Soeller. 2015. Examination of the effects of heterogeneous organization of RyR clusters, myofibrils and mitochondria on Ca^{2+} release patterns in cardiomyocytes. *PLoS Comput. Biol.* 11:e1004417.
3. Hatano, A., J. Okada, …, S. Sugiura. 2015. Distinct functional roles of cardiac mitochondrial subpopulations revealed by a 3D simulation model. *Biophys. J.* 108:2732–2739.
4. Song, Z., Z. Qu, and A. Karma. 2017. Stochastic initiation and termination of calcium-mediated triggered activity in cardiac myocytes. *Proc. Natl. Acad. Sci. USA.* 114:E270–E279.
5. Colman, M. A., C. Pinali, …, A. Kitmitto. 2017. A computational model of spatio-temporal cardiac intracellular calcium handling with realistic structure and spatial flux distribution from sarcoplasmic reticulum and t-tubule reconstructions. *PLoS Comput. Biol.* 13:e1005714.
6. Chamakuri, N., W. Neubert, …, M. Falcke. 2018. Multiscale modeling and numerical simulation of calcium cycling in cardiac myocytes. *SIAM Multiscale Modeling & Simulation.* 16:1115–1145.
7. Mirams, G. R., P. Pathmanathan, …, R. H. Clayton. 2016. Uncertainty and variability in computational and mathematical models of cardiac physiology. *J. Physiol.* 594:6833–6847.
8. Johnstone, R. H., E. T. Y. Chang, …, G. R. Mirams. 2016. Uncertainty and variability in models of the cardiac action potential: can we build trustworthy models? *J. Mol. Cell. Cardiol.* 96:49–62.
9. Krogh-Madsen, T., A. F. Jacobson, …, D. J. Christini. 2017. Global optimization of ventricular myocyte model to multi-variable objective improves predictions of drug-induced Torsades de Pointes. *Front. Physiol.* 8:1059.
10. Vagos, M. R., H. Arevalo, …, M. M. Maleckar. 2017. A computational framework for testing arrhythmia marker sensitivities to model parameters in functionally calibrated populations of atrial cells. *Chaos.* 27:093941.
11. Chang, E. T., M. Strong, and R. H. Clayton. 2015. Bayesian sensitivity analysis of a cardiac cell model using a Gaussian process emulator. *PLoS One.* 10:e0130252.
12. Renardy, M., T. M. Yi, …, C. S. Chou. 2018. Parameter uncertainty quantification using surrogate models applied to a spatial model of yeast mating polarization. *PLoS Comput. Biol.* 14:e1006181.
13. Xiu, D., and G. E. Karniadakis. 2002. The Wiener–Askey polynomial chaos for stochastic differential equations. *SIAM J. Sci. Comput.* 24:619–644.
14. Macquaide, N., H. T. Tuan, …, K. R. Sipido. 2015. Ryanodine receptor cluster fragmentation and redistribution in persistent atrial fibrillation enhance calcium release. *Cardiovasc. Res.* 108:387–398.
15. Xiu, D. 2009. Fast numerical methods for stochastic computations: a review. *Commun. Comput. Phys.* 5:242–272.
16. Jones, P. P., N. MacQuaide, and W. E. Louch. 2018. Dyadic plasticity in cardiomyocytes. *Front. Physiol.* 9:1773.
17. Jayasinghe, I., A. H. Clowsley, …, C. Soeller. 2018. True molecular scale visualization of variable clustering properties of ryanodine receptors. *Cell Rep.* 22:557–567.
18. Baddeley, D., I. D. Jayasinghe, …, C. Soeller. 2009. Optical single-channel resolution imaging of the ryanodine receptor distribution in rat cardiac myocytes. *Proc. Natl. Acad. Sci. USA.* 106:22275–22280.
19. Jayasinghe, I. D., M. B. Cannell, and C. Soeller. 2009. Organization of ryanodine receptors, transverse tubules, and sodium-calcium exchanger in rat myocytes. *Biophys. J.* 97:2664–2673.
20. Asghari, P., D. R. Scriven, …, E. D. Moore. 2014. Nonuniform and variable arrangements of ryanodine receptors within mammalian ventricular couplons. *Circ. Res.* 115:252–262.
21. Hou, Y., I. Jayasinghe, …, C. Soeller. 2015. Nanoscale analysis of ryanodine receptor clusters in dyadic couplings of rat cardiac myocytes. *J. Mol. Cell. Cardiol.* 80:45–55.
22. Walker, M. A., T. Kohl, …, R. L. Winslow. 2015. On the adjacency matrix of RyR2 cluster structures. *PLoS Comput. Biol.* 11:e1004521.
23. Galice, S., Y. Xie, …, D. M. Bers. 2018. Size matters: ryanodine receptor cluster size affects arrhythmogenic sarcoplasmic reticulum calcium release. *J. Am. Heart Assoc.* 7:e008724.
24. Shen, X., J. van den Brink, …, W. E. Louch. 2019. 3D dSTORM imaging reveals novel detail of ryanodine receptor localization in rat cardiac myocytes. *J. Physiol.* 597:399–418.
25. Cannell, M. B., C. H. Kong, …, D. R. Laver. 2013. Control of sarcoplasmic reticulum Ca^{2+} release by stochastic RyR gating within a 3D model of the cardiac dyad and importance of induction decay for CICR termination. *Biophys. J.* 104:2149–2159.
26. Walker, M. A., G. S. B. Williams, …, R. L. Winslow. 2014. Superresolution modeling of calcium release in the heart. *Biophys. J.* 107:3018–3029.
27. Bastian, P., M. Blatt, A. Dedner, C. Engwer, R. Klöfkorn, R. Kornhuber, M. Ohlberger, and O. Sander. 2008. A generic grid interface for parallel and adaptive scientific computing. Part II: implementation and tests in DUNE. *Computing.* 82:121–138.
28. Bastian, P., M. Blatt, A. Dedner, N.-A. Dreier, C. Engwer, R. Fritze, C. Gräser, D. Kempf, R. Klöfkorn, M. Ohlberger, and O. Sander. 2019. The DUNE framework: basic concepts and recent developments. *arXiv preprint*, arXiv:1909.13672.

29. Restrepo, J. G., and A. Karma. 2009. Spatiotemporal intracellular calcium dynamics during cardiac alternans. *Chaos.* 19:037115.

30. Nivala, M., E. de Lange, …, Z. Qu. 2012. Computational modeling and numerical methods for spatiotemporal calcium cycling in ventricular myocytes. *Front. Physiol.* 3:114.

31. Nivala, M., Z. Song, …, Z. Qu. 2015. T-tubule disruption promotes calcium alternans in failing ventricular myocytes: mechanistic insights from computational modeling. *J. Mol. Cell. Cardiol.* 79:32–41.

32. Schendel, T., and M. Falcke. 2010. Efficient and detailed model of the local Ca^{2+} release unit in the ventricular cardiac myocyte. *Genome Inform.* 22:142–155.

33. Schendel, T., R. Thul, …, M. Falcke. 2012. How does the ryanodine receptor in the ventricular myocyte wake up: by a single or by multiple open L-type Ca^{2+} channels? *Eur. Biophys. J.* 41:27–39.

34. Lanner, J. T., D. K. Georgiou, …, S. L. Hamilton. 2010. Ryanodine receptors: structure, expression, molecular details, and function in calcium release. *Cold Spring Harb. Perspect. Biol.* 2:a003996.

35. Iman, R. L., J. C. Helton, and J. E. Campbell. 1981. An approach to sensitivity analysis of computer models: Part I–Introduction, input variable selection and preliminary variable assessment. *J. Qual. Technol.* 13:174–183.

36. Mahajan, A., Y. Shiferaw, …, J. N. Weiss. 2008. A rabbit ventricular action potential model replicating cardiac dynamics at rapid heart rates. *Biophys. J.* 94:392–410.

37. Gemmell, P., K. Burrage, …, T. A. Quinn. 2016. Rabbit-specific computational modelling of ventricular cell electrophysiology: using populations of models to explore variability in the response to ischemia. *Prog. Biophys. Mol. Biol.* 121:169–184.

38. Box, G. E. 1980. Sampling and Bayes' inference in scientific modelling and robustness. *J. R. Stat. Soc. Ser. A.* 143:383–430.

39. Tran, D., A. Kucukelbir, …, D. M. Blei. 2016. Edward: a library for probabilistic modeling, inference, and criticism. *arXiv*, arXiv:1610.09787 https://arxiv.org/abs/1610.09787.

40. Abadi, M., P. Barham, …, X. Zheng. 2016. Tensorflow: a system for large-scale machine learning. In 12th USENIX Symposium on Operating Systems Design and Implementation, OSDI 2016, pp. 265–283.

41. Saltelli, A., and I. M. Sobol'. 1995. Sensitivity analysis for nonlinear mathematical models: numerical experience. *Matematicheskoe Modelirovanie.* 7:16–28.

42. Feinberg, J., and H. P. Langtangen. 2015. Chaospy: an open source tool for designing methods of uncertainty quantification. *J. Comput. Sci.* 11:46–57.

43. Sudret, B. 2008. Global sensitivity analysis using polynomial chaos expansions. *Reliab. Eng. Syst. Saf.* 93:964–979.

44. Williams, G. S., A. C. Chikando, …, M. S. Jafri. 2011. Dynamics of calcium sparks and calcium leak in the heart. *Biophys. J.* 101:1287–1296.

45. Takahashi, A., P. Camacho, …, B. Herman. 1999. Measurement of intracellular calcium. *Physiol. Rev.* 79:1089–1125.

46. Britton, O. J., A. Bueno-Orovio, …, B. Rodriguez. 2013. Experimentally calibrated population of models predicts and explains intersubject variability in cardiac cellular electrophysiology. *Proc. Natl. Acad. Sci. USA.* 110:E2098–E2105.

47. Neubauer, S. 2007. The failing heart–an engine out of fuel. *N. Engl. J. Med.* 356:1140–1151.

48. Ingwall, J. 2002. ATP and the Heart. Basic Science for the Cardiologist. Springer, New York.

49. Hake, J., A. G. Edwards, …, A. D. McCulloch. 2012. Modelling cardiac calcium sparks in a three-dimensional reconstruction of a calcium release unit. *J. Physiol.* 590:4403–4422.

Biophysical Journal, Volume *117*

Supplemental Information

Multiscale Modeling of Dyadic Structure-Function Relation in Ventricular Cardiac Myocytes

Filippo G. Cosi, Wolfgang Giese, Wilhelm Neubert, Stefan Luther, Nagaiah Chamakuri, Ulrich Parlitz, and Martin Falcke

Supplementary Material
Multi-scale modeling of dyadic structure-function relation in ventricular cardiac myocytes

Filippo G. Cosi, Wolfgang Giese, Wilhelm Neubert,
Stefan Luther, Nagaiah Chamakuri, Ulrich Parlitz, Martin Falcke*

*corresponding author: martin.falcke@mdc-berlin.de

Contents

1 Supplementary Text

Mathematical model

The mathematical model comprises several scales ranging from single receptors and ion channels to whole cell electrophysiology. The cell volume is described by a domain $\Omega \subset \mathbb{R}^3$ and the plasma membrane, meaning its boundary, by Γ. The dynamics of the cytosolic Ca^{2+} concentration, c, comprise plasma membrane transport, release and uptake by the SR and binding to buffers. Plasma membrane transport is carried by the voltage controlled ion channels and the NCX. The T-tubule network is an interface to the extracellular fluid in the bulk of the cytosol enabling membrane molecules like the NCX to contribute to bulk concentration dynamics (J_{NaCa}, see Eq (S1)). The term J_{pump} describes the pumping of Ca^{2+} by SERCAs into the SR. The Ca^{2+}-binding molecules ($b_j, j = s, m, f$) in the cytosol include stationary (s), mobile (m) and fluorescent (f) Ca^{2+} buffers. The total concentration b^j_{tot} is conserved for each of the buffers. The reaction terms $R_j(c, b_j)$ describe buffering in the dynamics of cytosolic Ca^{2+}. The partial differential equations for the cytosolic species are

$$\frac{\partial c}{\partial t} = \nabla \cdot (\mathbf{D}_c \nabla c) + J_{\mathrm{cru}} + J^{\mathrm{vol}}_{\mathrm{NCX}} + J_{\mathrm{leak}} - J_{\mathrm{pump}} - \sum_{j=m,s,f} R_j(c, b_j) \quad \text{in } \Omega \times [0, T], \tag{S1}$$

$$\frac{\partial b_j}{\partial t} = \nabla \cdot (\mathbf{D}^j_b \nabla b_j) + R_j(c, b_j), \qquad j = s, m, f \quad \text{in } \Omega \times [0, T], \tag{S2}$$

where $\mathbf{D}$ and $\mathbf{D}^j_b$ are diagonal diffusion matrices. In the current implementation, isotropic diffusion is assumed. The expressions for the fluxes are

$$J_{\mathrm{cru}} = \sum_{i=1}^{N_{\mathrm{cru}}} \Theta(R^i_{\mathrm{cru}} - |\mathbf{r} - \mathbf{r}_i|) J^i_c(c, V_m, t), \tag{S3}$$

$$J_{\mathrm{leak}} = V_l(c_{\mathrm{sr}} - c), \tag{S4}$$

$$J_{\mathrm{pump}} = V^{\max}_p \frac{c}{K_p + c} \frac{c_{\mathrm{sr},0}}{c_{\mathrm{sr}}}, \tag{S5}$$

$$R_j(c, b_s, \mathbf{r}) = k^+_j (b^{\mathrm{tot}}_m - b_m)c - k^-_m b_m, \tag{S6}$$

where $\Theta(x)$ is the Heaviside step function, k_j^+ and k_j^- are the binding and dissociation rates for the buffer j (for $j = m, s, f$). Ca^{2+} influx through LCC (I_{LCC}) and release through RyR (I_{RyR}) channels occur mainly in dyadic clefts (J_{cru}). The dependence on time of J_{cru} is caused by their stochastic behavior.

The space inside CRUs is described as a flat cylinder in the detailed CRU model. The interface between dyadic space and cytosol through which Ca^{2+} leaves the CRU is a band twisted in 3 dimensions since the jSR wraps around T-tubules. Since we cannot represent the shape of this interface for each CRU on the level of the PDEs, its geometry is approximated as spherical source volume centered at $\mathbf{r}_i$ with radius R^i_{cru} and random flux $J^i_c(c(\mathbf{r}_i), V_m, t)$. The flux $J^i_c(c, V_m, t)$ is the sum of all single channel LCC- and RyR-currents in the ith CRU divided by $\frac{4}{3}\pi \left(R^i_{\mathrm{cru}}\right)^3$.

The boundary conditions for the above PDEs are given by the plasma membrane Ca^{2+}-currents

$$\mathbf{n} \cdot \mathbf{D}_c \nabla c = J^{pm}_{\mathrm{NCX}} \text{ on } \Gamma \times [0, T], \tag{S7}$$

$$\mathbf{n} \cdot \mathbf{D}_{b_j} \nabla b_j = 0 \text{ on } \Gamma \times [0, T], \tag{S8}$$

where J^{pm}_{NCX} is the plasma membrane part of the NCX flux. Ca^{2+} is released into dyadic clefts from specialized parts of the sarcoplasmic reticulum called junctional sarcoplasmic reticulum (jSR). The jSR of the individual CRUs are coupled to the network SR by a diffusional flux

$$J_{\mathrm{jsr}} = \sum_{i=1}^{N_c} \frac{\Theta(R^i_{\mathrm{jsr}} - |\mathbf{r} - \mathbf{r}_i|) I_{\mathrm{refill},i}}{\frac{4}{3}\pi \left(R^i_{\mathrm{jsr}}\right)^3}. \tag{S9}$$

$I_{\mathrm{refill,i}}$ denotes the current from the network SR to the ith jSR. The radius of the sink volume in the lumen of the SR is R^i_{jsr}. This flux and a stationary buffer contribute to SR Ca^{2+} concentration dynamics

$$\frac{\partial c_{\mathrm{sr}}}{\partial t} = \nabla \cdot (\mathbf{D}_{\mathrm{sr}} \nabla c_{\mathrm{sr}}) - J_{\mathrm{jsr}} + \frac{\nu_{\mathrm{sr}}}{\nu_{cyt}} (J_{\mathrm{pump}} - J_{\mathrm{leak}}) \text{ in } \Omega \times [0, T]. \tag{S10}$$

$\mathbf{D}_{\mathrm{sr}}$ is the diffusion coefficient for the SR Ca^{2+} concentration. The bi-domain approximation for cytosol and SR is used [12]. In this concept both compartments occupy the same volume continuously with volume ratio $\nu_{\mathrm{sr}}/\nu_{\mathrm{cyt}}$. A zero-flux Neumann boundary condition for the SR Ca^{2+} is imposed on the domain boundary.

The RyR state transitions are determined according to a fixed closing rate, k_{close}, and an opening rate given by

$$k_{\mathrm{open}} = k_{\mathrm{plus}} \phi c^{\eta}_{\mathrm{di}}, \text{ with } \phi = \phi_b + \left(\frac{c_{\mathrm{jsr}}}{\phi_k}\right)^4. \tag{S11}$$

The number of RyRs N^i_{RyR} in the ith CRU is drawn from the distribution $P(N)$

$$P(N) = \begin{cases} \frac{1}{N_N} e^{-\frac{N}{N_{\mathrm{RyR}}}}, & 8 \le N \le 80 \\ 0, & \text{otherwise} \end{cases}. \tag{S12}$$

N_N normalizes the distribution. The upper cutoff was chosen because the size distribution measured in ref [11] has well declined at this value and channel numbers larger than 80 lead in combination with the placement algorithm to large CRUs, larger than a typical CRU-CRU-distance.

We use previously developed CRU model [16], which has a spatially resolved description of the dyadic cleft channel placement and representation of the jSR. The dyadic cleft is assumed to be a cylinder with a height of 15 nm, where the RyRs at the jSR membrane are co-localized to the LCCs at the T-tubule membrane. The behaviour of the CRU is mainly governed by three different dynamics: the gating of the main Ca^{2+} -channels (LCCs and RyRs), the Ca^{2+}-profile within the dyadic cleft and the Ca^{2+}-dynamics of the jSR.

The Ca^{2+} concentration in the cleft (c_{di}) is modeled by a partial differential equation in cylindrical coordinates [4, 15, 16, 19]

$$\frac{\partial c_{\mathrm{di}}}{\partial t} = \sum_{k=1}^{N^i_{\mathrm{LCC}}} I^k_{\mathrm{LCC}} \delta(\mathbf{r} - \mathbf{r_k}) + \sum_{k=1}^{N^i_{\mathrm{RyR}}} I^k_{\mathrm{RyR}} \delta(\mathbf{r} - \mathbf{r_k}) + D_c \Delta_{r,\varphi} c_{\mathrm{di}}(\mathbf{r}) - \frac{\partial}{\partial z} J_z. \tag{S13}$$

The electro-diffusive flux resulting from membrane surface charges is J_z and takes the buffering effect of membranes into account.

The Ca^{2+} concentration is computed from a quasi-steady state approximation for this equation. It is quasi-steady since changes of the jSR-concentration affecting RyR currents and the boundary conditions at the rim of the cleft are taken into account [4]. The stationary solution for given boundary conditions and jSR concentration is

$$c_{\mathrm{di}}(\mathbf{r}) = Z(z_i)c_{\mathrm{bulk}} + \sum_{k=1}^{N^i_{\mathrm{LCC}}} I^k_{\mathrm{LCC}}\eta(\mathbf{r}_k,\mathbf{r}) + \sum_{j=1}^{N^i_{\mathrm{RyR}}} I^j_{\mathrm{RyR}}\eta(\mathbf{r}_j,\mathbf{r}). \tag{S14}$$

with

$$\eta(\mathbf{r}_i,\mathbf{r}) = \frac{Z(z)}{\beta_d h^* D_c} G((r,\phi),(\rho_i,\phi_i)), \tag{S15}$$

where $Z(z) = \exp(-2\phi_0 \exp(-\kappa z))$ describes the gradient resulting from electrodiffusion [4, 15, 16, 19], $h^* = \int_0^h dz Z(z)$ and β_d is a constant buffering factor. The boundary conditions are determined by the bulk Ca^{2+} concentration averaged over the boundary of the dyadic space. $G((r,\phi),(\rho_i,\phi_i))$ is Green's function. Since the RyR- and LCC-currents depend on the local Ca^{2+} concentration at the channel mouths, we cannot use a superposition of single channel Green's functions but Eq. S14 defines a system of linear algebraic equations realizing the coupling of currents by dyadic diffusion and providing the local concentration values [4, 15, 16, 19].

We do not know any experimental results on the correlation between RyR number and the size of the dyadic space. Hence, we made the assumption that the radius of the dyadic space is such that the RyR cluster determined from the placement model can be accommodated with a minimum distance between any RyR and the cleft boundary of 60 nm.

The RyR-currents are proportional to the concentration difference $c_{\mathrm{jsr,i}} - c_{\mathrm{di}}$ [4, 15, 16, 19]. The concentration of $c_{\mathrm{jsr,i}}$ in the ith jSR obeys an ordinary differential equation [4, 19]:

$$\frac{dc_{\mathrm{jsr,i}}}{dt} = \frac{1}{\beta_{\mathrm{jsr}}\nu_{\mathrm{jsr,i}}}\left(I_{\mathrm{refill}} - \sum_{j=1}^{N^i_{\mathrm{RyR}}} I^j_{\mathrm{RyR}}\right) \tag{S16}$$

$$I_{\mathrm{refill}} = \frac{S(\mathbf{r_i}) - c_{\mathrm{jsr,i}}}{\tau_{\mathrm{refill}}}\nu_{\mathrm{jsr,i}} \tag{S17}$$

$$\beta_{\mathrm{jsr}} = 1 + \frac{nK_{\mathrm{csqn}}B_{\mathrm{csqn}}}{(K_{\mathrm{csqn}} + c_{\mathrm{jsr,i}})^2}. \tag{S18}$$

Details are explained in ref. [4]. I_{refill} is the diffusive current from the network SR. The factor β_{jsr} describes buffering by Calsequestrin.

The electrophysiology is based on Mahajan et al. [14] and was adapted to the above CRU modelling concept. The dynamics of the membrane potential V_m is given by:

$$\frac{dV_m}{dt} = -(I_{\mathrm{ion}} + I_{\mathrm{stim}}). \tag{S19}$$

Here, I_{stim} is the current to depolarize the cell. The ion current is given by

$$I_{\mathrm{Ion}} = I_{\mathrm{Na}} + I_{\mathrm{to,f}} + I_{\mathrm{to,s}} + I_{\mathrm{Kr}} + I_{\mathrm{Ks}} + I_{\mathrm{K1}} + I_{\mathrm{NaK}} + I_{\mathrm{CaL}} + I_{\mathrm{NCX}}, \tag{S20}$$

where I_{Na} is the fast Na^+ current, $I_{\mathrm{to,f}}$ is the fast and $I_{\mathrm{to,s}}$ the slow component of the rapid outward K^+ current, I_{Kr} is the rapid delayed rectifier current, I_{Ks} is the slow delayed rectifier current, I_{K1} is the inward rectifier current, and I_{NaK} is the Na^+/K^+-pump current.

The LCC current is denoted by I_{CaL} (mV/ms), which is the sum of all LC channel currents over all CRUs in the model. The NCX current I_{NCX} (mV/ms), is the integral of the local flux J_{NCX} over the simulation domain and its boundary.

Numerical methods

Due to the presence of multiple scales in space and time, the stochasticity of CRU behaviour and the coupling of partial differential equations (PDEs) for concentrations and ordinary differential equations (ODEs) for the membrane potential the model exhibits some challenges with respect to numerical methods. Therefore, we dedicated previous studies to develop numerical methods living up to these requirements [19, 4]. In particular the recent study [4] published in the applied mathematics journal SIAM Multiscale Modelling & Simulations describes the methods used in this study and explains and motivates all the numerical methods in detail. Here, we provide a short overview only.

For the vast majority of complex geometries and model problems, the PDEs cannot be solved with analytical methods. Instead, an approximation of the equations can be constructed, typically based upon different types of numerical methods. We use the Finite Element Method (FEM), which is arguably the most powerful method known for the numerical solution of boundary- and initial-value problems characterized by partial differential equations. The spatial discretization of the given PDEs by the finite element method leads to a system of ODEs for transient problems. To solve such ODEs, we use an adaptive higher order Runge-Kutta time-stepping scheme, specifically the ROWDA3 [13] method. At each time step of the ROWDA3 method, the discretized model equations lead to a set of algebraic equations which are solved by a biconjugate gradient stabilized method (BiCGSTAB) [18] with ILU preconditioner.

We use the forward Euler method for the membrane potential dynamics and Rush-Larsen time step integrator for the gating and concentration equations. Our numerical schemes are implemented in C++ and were developed based on the public domain FEM package DUNE [1] and Dune-PDELab [2], which allows for highly parallelized computations. Computations were performed on the high performance compute cluster at the Max Delbrück Center for Molecular Medicine in Berlin as well as at the Max Planck Institute for Dynamics and Self-Organization in Göttingen. AP simulations were performed on 4 InfiniBand or OmniPath nodes with 16 cores each, where each simulation takes about 30 h to simulate 15 APs. Spark simulations were performed on 8 InfiniBand or OmniPath nodes, where each simulation took about 36 h.

Error estimates for polynomial chaos expansion

The least-square fit error determines the regression error of the whole data set, the cross-validation error describes over-fitting by splitting the data set into training- and test-data. Here we used a k-fold method with (k=10) for cross validation [10]. Let $\mathcal{I}$ be an index subset of $\{1, \ldots, N\}$, where N is number of data points. The R^2-score is defined as

$$R^2 = 1 - \frac{\sum_{i\in\mathcal{I}}(Y_i - \hat{Y}_i)^2}{\sum_{i\in\mathcal{I}}(Y_i - \bar{Y})^2}. \tag{S21}$$

Here, Y_i denotes the actual biomarker output from the simulations, $\hat{Y}_i$ the value from the polynomial regression and $\bar{Y}$ is the mean value of the data points in the data set. The coefficient of determination is calculated from the R^2-score for the whole data set, meaning $\mathcal{I} \equiv \{1, \ldots, N\}$. In case of the cross-validation coefficient, we calculated the average of the R^2-score from the test-sets, which arises from the splitting of the data-set by the k-fold method.

We furthermore penalized the number of coefficients by employing the commonly used LASSO (least absolute shrinkage and selection operator) method using a python library for machine learning called `scikit-learn` We determined the polynomial degree as well as the penalty parameter for the lasso method, which result in minimal cross-validation error for each biomarker. In Figure S2, the coefficient of determination, cross-validation coefficient and the mean absolute percentage error (MAPE) are shown for APD_{90}. The MAPE is defined as

$$\text{MAPE} = \frac{100\%}{n}\sum_{i=1}^{n}\left|\frac{Y_i - \hat{Y}_i}{Y_i}\right|. \tag{S22}$$

Note the MAPE comprises uncertainty in the model output and regression error. Since the model is stochastic, the output cannot be predicted with absolute certainty and, therefore, the MAPE is not converging to zero even if the mean is described well by the polynomial regression.

References

[1] P. Bastian, M. Blatt, A. Dedner, C. Engwer, R. Klöfkorn, R. Kornhuber, M. Ohlberger, and O. Sander. A generic grid interface for parallel and adaptive scientific computing. Part II: implementation and tests in DUNE. *Computing*, 82(2):121–138, 2008.

[2] P. Bastian, F. Heimann, and S. Marnach. Generic implementation of finite element methods in the distributed and unified numerics environment (DUNE). *Kybernetika*, 46(2):294–315, 2010.

[3] Marco Bertamini, Michele Zito, Nicholas E. Scott-Samuel, and Johan Hulleman. Spatial clustering and its effect on perceived clustering, numerosity, and dispersion. *Attention, Perception, & Psychophysics*, 78(5):1460–1471, Jul 2016.

[4] N. Chamakuri, W. Neubert, S. Gilbert, J. Vierheller, G. Warnecke, and M. Falcke. Multiscale modeling and numerical simulation of calcium cycling in cardiac myocytes. *SIAM Multiscale Modeling & Simulation*, 16(3):1115–1145, 2018.

[5] Heping Cheng and WJ Lederer. Calcium sparks. *Physiological Reviews*, 88(4):1491–1545, 2008.

[6] D Fedida and WR Giles. Regional variations in action potentials and transient outward current in myocytes isolated from rabbit left ventricle. *The Journal of Physiology*, 442(1):191–209, 1991.

[7] Philip Gemmell, Kevin Burrage, Blanca Rodríguez, and T Alexander Quinn. Rabbit-specific computational modelling of ventricular cell electrophysiology: Using populations of models to explore variability in the response to ischemia. *Progress in Biophysics and Molecular Biology*, 121(2):169–184, 2016.

[8] Joshua I Goldhaber, Scott T Lamp, Donald O Walter, Alan Garfinkel, Gary H Fukumoto, and James N Weiss. Local regulation of the threshold for calcium sparks in rat ventricular myocytes: role of sodium-calcium exchange. *The Journal of physiology*, 520(2):431–438, 1999.

[9] David A Golod, Rajiv Kumar, and Ronald W Joyner. Determinants of action potential initiation in isolated rabbit atrial and ventricular myocytes. *American Journal of Physiology-Heart and Circulatory Physiology*, 274(6):H1902–H1913, 1998.

[10] Trevor Hastie, Robert Tibshirani, and Jerome Friedman. *The elements of statistical learning: data mining, inference, and prediction, Springer Series in Statistics*. Springer New York, 2009.

[11] Isuru Jayasinghe, Alexander H. Clowsley, Ruisheng Lin, Tobias Lutz, Carl Harrison, Ellen Green, David Baddeley, Lorenzo Di Michele, and Christian Soeller. True molecular scale visualization of variable clustering properties of ryanodine receptors. *Cell Reports*, 22(2):557 – 567, 2018.

[12] James P Keener and James Sneyd. *Mathematical physiology I: Cellular Physiology*. Springer, 2nd ed., 2009.

[13] J. Lang. *Adaptive Multilevel Solution of Nonlinear Parabolic PDE Systems*, volume 16 of *Lecture Notes in Computational Science and Engineering*. Springer-Verlag, Berlin, 2001.

[14] Aman Mahajan, Yohannes Shiferaw, Daisuke Sato, Ali Baher, Riccardo Olcese, Lai-Hua Xie, Ming-Jim Yang, Peng-Sheng Chen, Juan G Restrepo, Alain Karma, et al. A rabbit ventricular action potential model replicating cardiac dynamics at rapid heart rates. *Biophysical Journal*, 94(2):392–410, 2008.

[15] Thomas Schendel and Martin Falcke. Efficient and detailed model of the local Ca^{2+} release unit in the ventricular cardiac myocyte. *Genome Informatics*, 22:142–155, 2009.

[16] Thomas Schendel, Rüdiger Thul, James Sneyd, and Martin Falcke. How does the ryanodine receptor in the ventricular myocyte wake up: by a single or by multiple open l-type Ca^{2+} channels? *European Biophysics Journal*, 41(1):27–39, 2012.

[17] Yohannes Shiferaw. Nonlinear onset of calcium wave propagation in cardiac cells. *Physical Review E*, 94(3):032405, 2016.

[18] H. A. van der Vorst. Bi-CGSTAB: A fast and smoothly converging variant of bi-cg for the solution of nonsymmetric linear systems. *SIAM J. Sci. Stat. Comput.*, 13:631–644, 1992.

[19] Janine Vierheller, Wilhelm Neubert, Martin Falcke, Stephen Henry Gilbert, and Nagaiah Chamakuri. A multiscale computational model of spatially resolved calcium cycling in cardiac myocytes: from detailed cleft dynamics to the whole cell concentration profiles. *Frontiers in Physiology*, 6:255, 2015.

[20] Mark A Walker, George SB Williams, Tobias Kohl, Stephan E Lehnart, M Saleet Jafri, Joseph L Greenstein, WJ Lederer, and Raimond L Winslow. Superresolution modeling of calcium release in the heart. *Biophysical Journal*, 107(12):3018–3029, 2014.

2 Supplementary Tables

Table S1: Literature biomarker ranges for Ca^{2+} transients and action potentials. Note that for the values from [9], the standard deviation was calculated from the standard error by $\sigma = \sqrt{n}\hat{\sigma}$. See also Fig. S6.

	target values (literature)	description
Biomarker (AP)		
max V_m	46 ± 4.5 mV [9]	maximal value of action potential peaks
resting V_m	-82.7 ± 1.4 mv [9], ≈ $-85mV$ [14], -81.3 ± 3.9 mV [6]	resting value of the action potential
amplitude (V_m)	127 ± 2.0 mV [9]	difference of resting potential and max V_m
amplitude (dome)	96.5 ± 9.3 mV [6]	difference of resting potential and dome V_m
dome V_m	15.2 ± 10.1 mV [6]	peak in the plateau phase
dV_m/dt	395 ± 47 V/s [9]	maximum rate of rise of the action potential
APD_{50}	104 ms - 117 ms (at 400 ms PCL) [7]	action potential duration at 50%
APD_{90}	142 ms - 188 ms (at 400 ms PCL) [7]	action potential duration at 90%
systolic $[Ca^{2+}]$	0.8 µM - 1.5 µM (at 400 ms PCL)	peak systolic calcium
diastolic $[Ca^{2+}]$	0.15 µM - 0.3 µM (at 400 ms PCL)	diastolic calcium
$[Na^{+}]_i$	10.5 mM - 11.5 mM (at 350 ms PCL) [14]	intracellular sodium
Biomarker (Spark)		
FDHM	8.4 ± 0.5 ms [8] ,≈ 15 ms [17], ≈ 30 ms [5]	full duration at half maximum of a spark
peak $[Ca^{2+}]_i^{exp}$	≈ 1 µM [5]	peak of experimental Ca^{2+} concentration inferred from fluo4 during a spark
peak $[Ca^{2+}]_i$	≈ 10 µM [20]	underlying local peak Ca^{2+} concentration
spark rate	1 $s^{-1}\mu m^{-1}$ [5]	number of spark per section cell (in µm, longitudinal direction) and time (in seconds)

Table S2: Dyadic cleft parameters.

Parameter	Meaning	Value
N_{RyR}	distribution parameter for RyRs per dyadic cleft	20
N_{LCC}	average number of LCCs per dyadic cleft	4
$r_{\mathrm{RyR,LCC}}$	ratio of RyRs and LCCs	5
k_{plus}	rate constant determining the RyR opening rate	varies
k_{close}	closing rate (RyRs)	varies
ϕ_k	$[Ca^{2+}]_{jsr}$- dependent regulation affinity	1.59 mM
ϕ_b	$[Ca^{2+}]_{jsr}$- dependent regulation minimum	0.8025
η	c_{di} sensitivity Hill Coefficient	2.1
μ_{RyR}	step length distribution parameter for average of RyR placement	40.1 nm
σ_{RyR}	step length distribution parameter for standard deviation of RyR placement	7.4 nm
r_{min}	minimum distance for placement	30 nm
r_{chb}	minimum RyR distance to cleft boundary	60 nm
g_{RyR}	RyR permeability	varies

Table S3: Exchanger and uptake parameters.

Parameter	Meaning	Value
g_{NaCa}	strength of Na^+/Ca^{2+}-exchanger	1.8 µM s^{-1}
$f_{\mathrm{NaCa,high}}$	maximal factor for g_{NaCa} at dyadic cleft centers	72.0
$f_{\mathrm{NaCa,low}}$	minimal factor for g_{NaCa} distant to dyadic clefts	0.66
$f_{\mathrm{NaCa,surf}}$	minimal factor for g_{NaCa} at cell surface	0.5
$V_{\mathrm{P,max}}$	maximal rate of SERCA uptake	varies
K_{P}	SERCA uptake threshold	0.4 µM
k_{sat}	constant	0.2
ξ	constant	0.35
$K_{\mathrm{m,Nai}}$	constant	12.3 mM
$K_{\mathrm{m,Na0}}$	constant	87.5 mM
$K_{\mathrm{m,Cai}}$	constant	3.6×10^{-3}
$K_{\mathrm{m,Cao}}$	constant	1.3 mM
c_{naca}	constant	0.3 µM

Table S4: Constants involved in computing transition rates for LCC channels.

Parameter	Meaning	Value
s_1'	voltage-inactivation rate	0.00195 ms^{-1}
r_2	closing rate	3.0 ms^{-1}
k_p^0	half-rate Ca^{2+} binding constant	180.0 μM
τ_{po}	average closed time	1.0 ms
r_1	uninhibited open rate	0.3 ms
k_1'	voltage-inhibition rate	0.00413 ms^{-1}
T_{Ba}	fitting parameter	450.0 ms
k_2	Ca^{2+} unbinding rate (LCCs)	1.03615×10^{-4} ms^{-1}
k_2'	voltage-Inhibition resolution rate	2.24×10^{-4} ms^{-1}
$\bar{c_p}$	half-rate constant for deep Ca^{2+} inhibition	60.0 μM
g_{LCC}	LCC permeability	varies

Table S5: Constants relevant to diffusion model inside the dyadic space.

Parameter	Meaning	Value
ϕ_0	dimensionless constant	-2.2
κ	inverse of the Debye length	1 nm^{-1}
D_c	diffusion constant for Ca^{2+} in the dyadic space	0.1 $\mu m^2 ms^{-1}$
h	height of the dyadic space cylinder	15 nm
R	radius of the dyadic space cylinder	varies
R_B	universal gas constant	8.31 $kJ(K\ mol)^{-1}$
T	temperature of the cell	308 K
β_d	buffering factor	2

Table S6: Constants and parameters involved in modelling the Ca^{2+} dynamics in the jSR.

Parameter	Meaning	Value
B_{csqn}	total calsequestrin concentration	800 μM
n	number of calsequestrin binding sites	15
K_{csqn}	dissociation constant of calsequestrin	600 μM
ν_{jSR}	volume of the jSR	varies
τ_{refill}	refill flux time constant	0.5 ms

Table S7: Buffering and diffusion parameters.

Parameter	Description	Value
b_m^{tot}	total concentration of calmodulin (mobile buffer)	25.0 µM
b_s^{tot}	total concentration of troponin C (stationary buffer)	70.0 µM
B_{sr}^{tot}	total concentration of jSR buffer	1500.0 µM
b_{Fluo-4}^{tot}	total concentration of Fluo-4	25.0 µM
D_c	diffusion constant of cytosolic Ca^{2+}	0.22 $\frac{\mu m^2}{ms}$
D_{b_m}	diffusion constant of calmodulin	0.04 $\frac{\mu m^2}{ms}$
D_{b_s}	diffusion constant of troponin C	0 $\frac{\mu m^2}{ms}$
D_{b_f}	diffusion constant of Fluo-4	0.033 $\frac{\mu m^2}{ms}$
D_S	diffusion constant of sarcoplasmic Ca^{2+}	0.2 $\frac{\mu m^2}{ms}$
k_s^+	on rate for troponin C binding	0.043 μM^{-1} ms^{-1}
k_s^-	off rate for troponin C binding	0.026 ms^{-1}
k_m^+	on rate for calmodulin binding	0.023 μM^{-1} ms^{-1}
k_m^-	off rate for calmodulin binding	0.238 ms^{-1}
ν_{sr}/ν_{cell}	ratio of SR to cell volume	0.08
ν_{jsr}/ν_{cell}	ratio of jSR to cell volume	0.005
ν_{cyt}/ν_{cell}	ratio of cytosolic volume to cell volume	0.915

Table S8: Initial Values.

Parameter	Description	Value
c	free cytoplasmic Ca^{2+} concentration	0.1 µM
b_x	buffered cytosolic Ca^{2+} (for $x = m, s, f$)	$\frac{b_x^{tot} \cdot c}{k_x^+/k_x^- + c}$
S	free sarcoplasmic Ca^{2+} concentration	1200 µM

Table S9: Ionic current conductances.

Parameter	Meaning	Value
g_{Na}	peak I_{Na} conductance	12.0 mS/µmF
$g_{to,f}$	peak $I_{to,f}$ conductance	0.11 mS/µmF
$g_{to,s}$	peak $I_{to,s}$ conductance	0.04 mS/µmF
g_{K1}	peak I_{K1} conductance	0.3 mS/µmF
g_{Kr}	peak I_{Kr} conductance	0.0125 mS/µmF
g_{Ks}	peak I_{Ks} conductance	0.1386 mS/µmF
g_{NaK}	peak I_{Kr} conductance	1.5 mS/µmF

3 Supplementary Figures

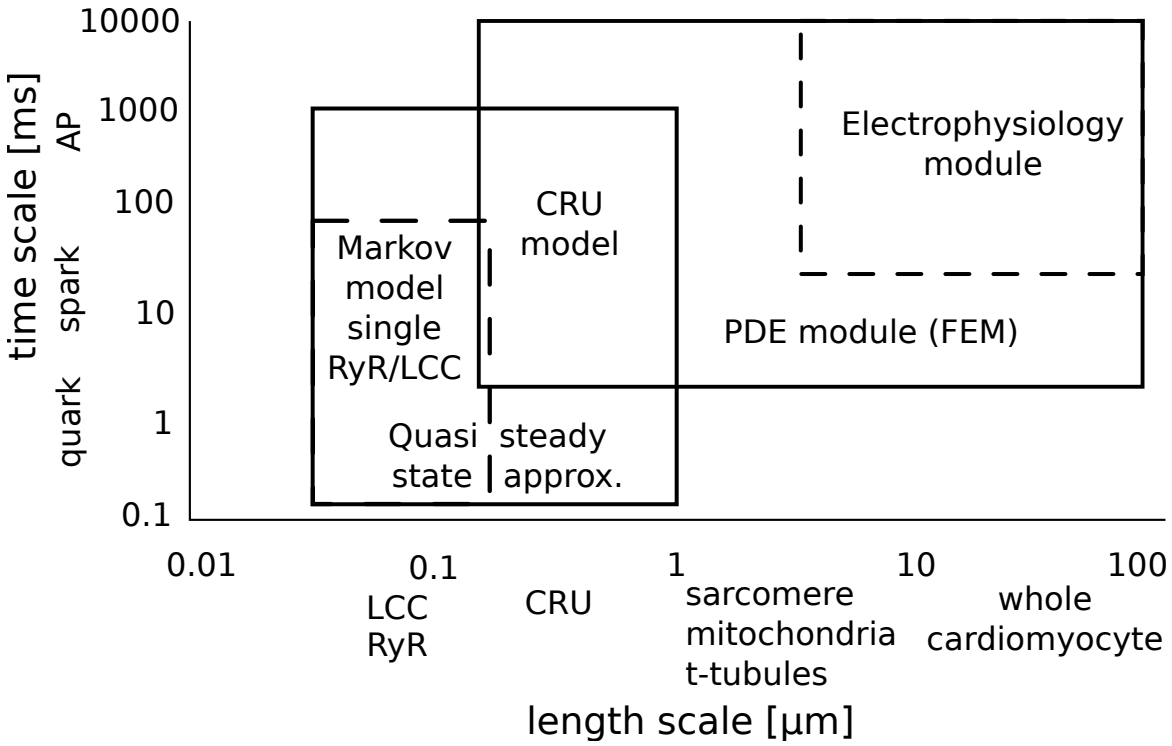

Figure S1: The mathematical model covers several spatial and temporal scales. On the shortest length and time scales a quasi-steady state approximation for the dyadic concentration profiles and a Markov model for the individual channels is employed to model Ca^{2+} dynamics on the spatial and temporal scales in the dyadic cleft. The PDE module links the whole cell electrophysiology to the signalling in the local CRU micro-domain.

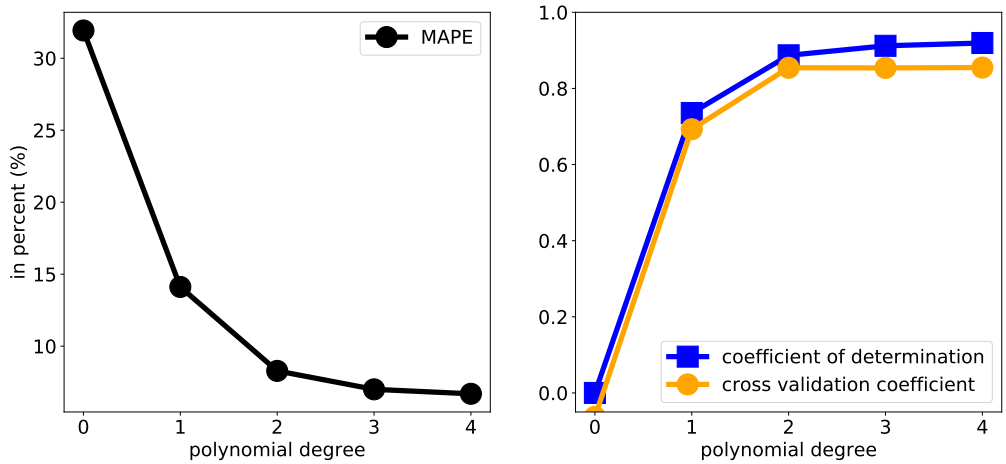

Figure S2: The mean absolute percentage error (MAPE), the coefficient of determination and the cross validation error for the example of the systolic peak Ca^{2+} biomarker.

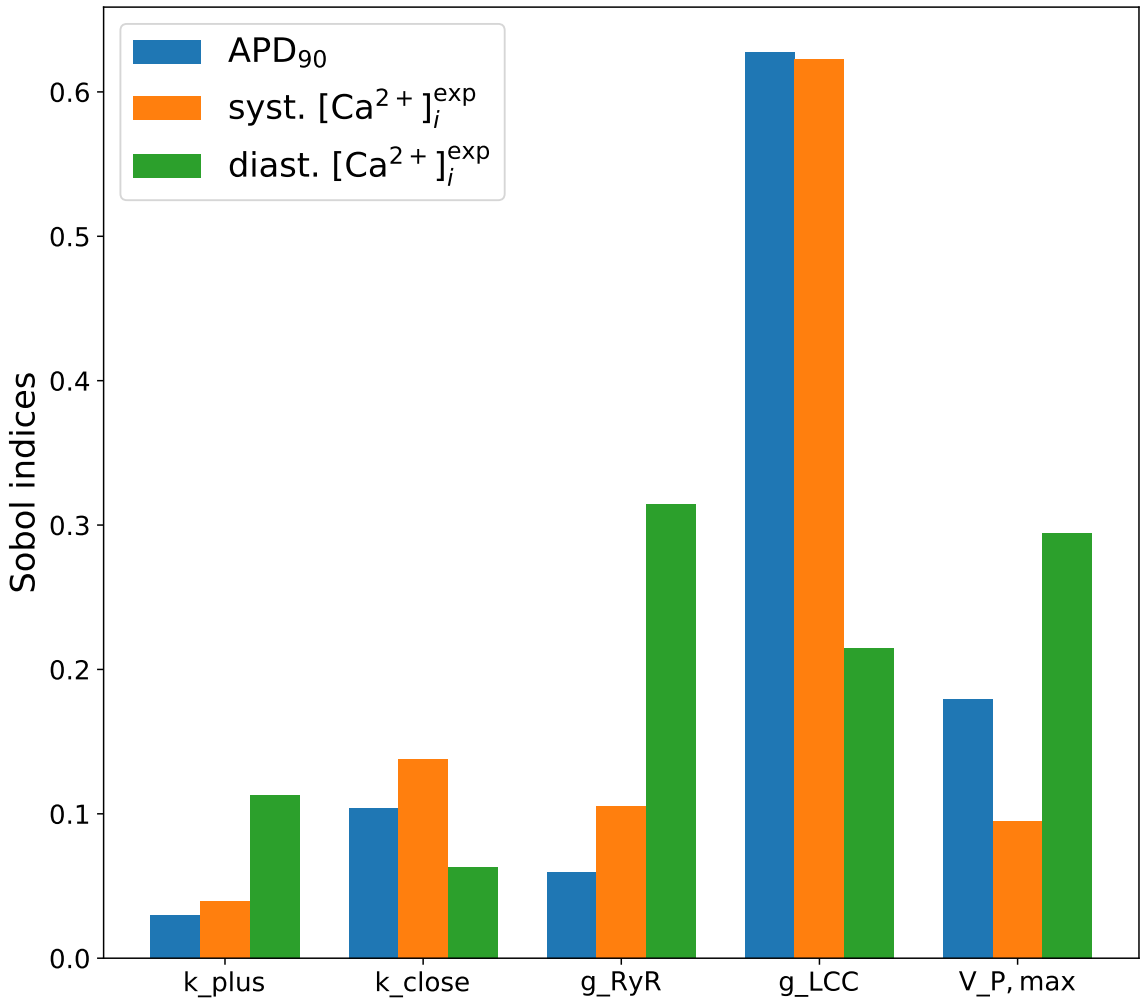

Figure S3: Calculation of Sobol indices as a measure for global sensitivities for action potential biomarkers.

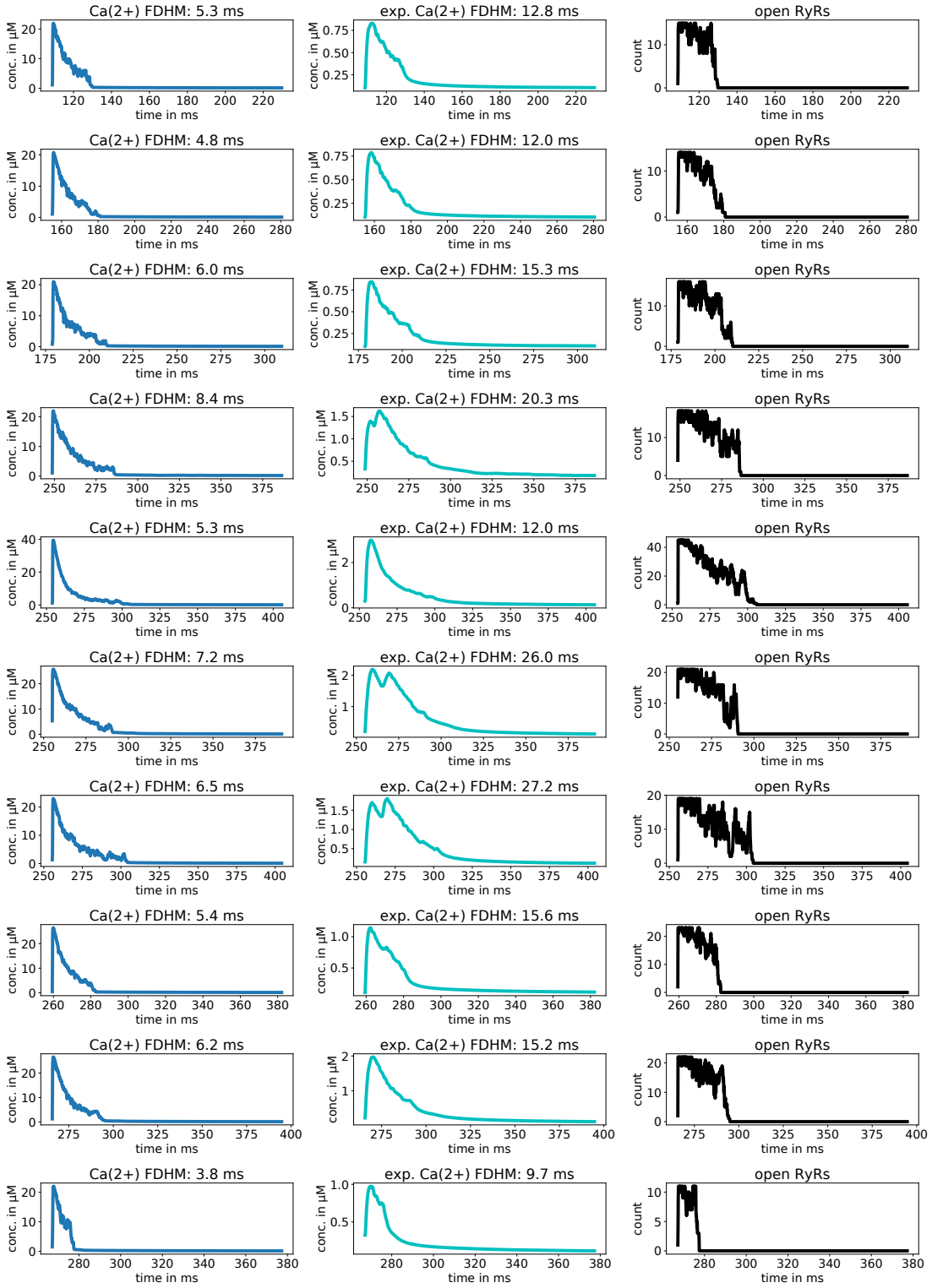

Figure S4: Comparison of experimental Ca^{2+} inferred from the buffer and the underlying simulated Ca^{2+}.

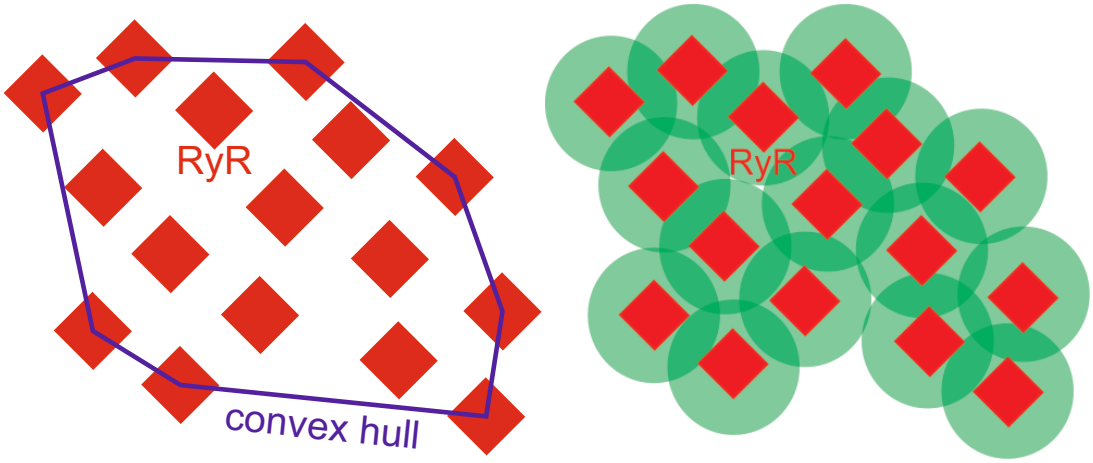

Figure S5: Left panel: We determine the area per channel using the concept of convex hull [3]. The hull wraps around the channels of a cluster like a police line around a group of tress does. The line goes through the center point of channels. The area per channel is determined as the area inside the convex hull divided by the number of channels. Note, channels on the hull contribute less to the area than inner channels. Hence, the channel per area is smaller than the square of the channel distance in a regular quadratic configuration of channels. Specifically we used https://docs.scipy.org/doc/scipy/reference/generated/scipy.spatial.ConvexHull.html. Right panel: A circular area of influence (green) is appointed to each channel. We denote the sum of the areas of influence of all channels with Σ and the sum of all overlap areas with Ω. The mean occupancy is defined as 1-Ω/Σ [3]. Mean occupancy is small, if channels are close to each other and the overlap is large. The regular placement has smaller mean occupancy (≈ 0.36) than the placement according to Jayasinghe et al. (mean occupancy ≈ 0.49) with measured parameters from [11].

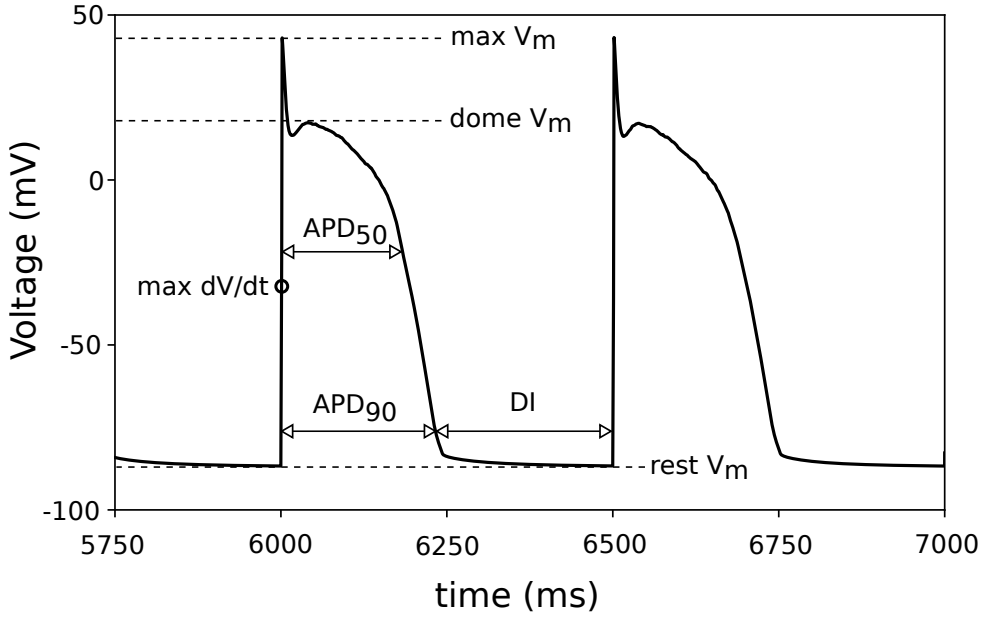

Figure S6: Action potential (AP) characterization.

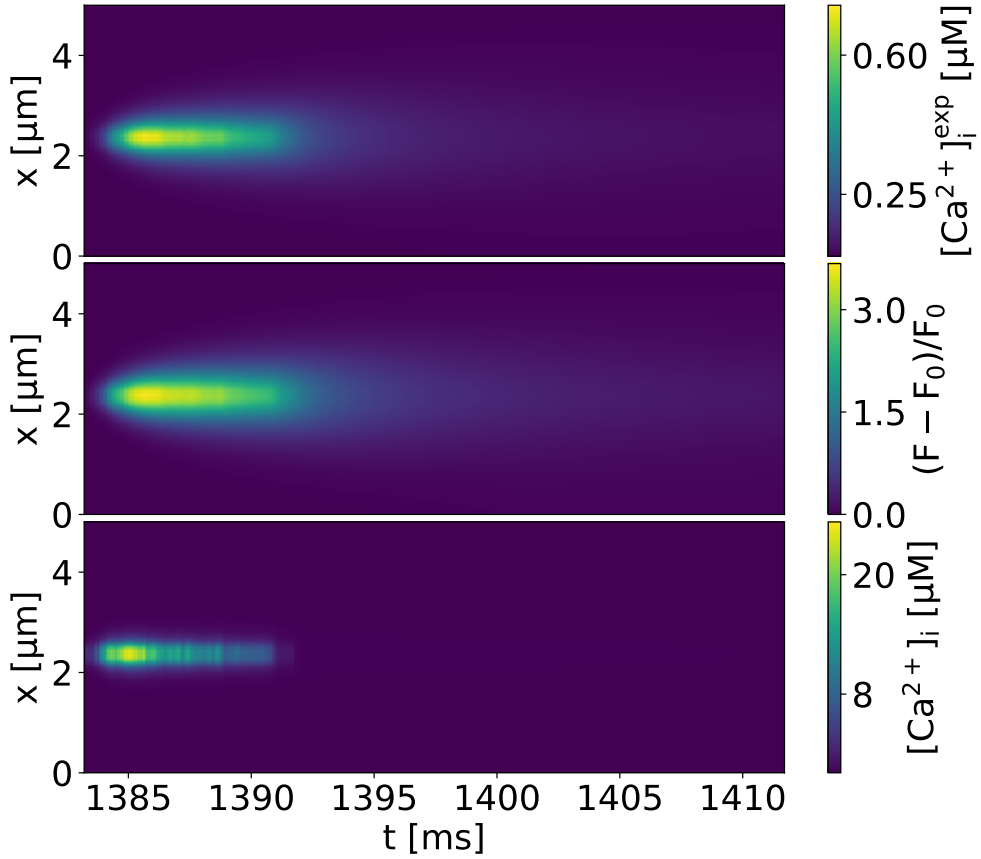

Figure S7: Example linescans of a spark in a 2.5 µm surrounding of a CRU. Shown are the concentrations of Fluo-4 bound Ca^{2+} and cytosolic Ca^{2+} in the upper and lower panel respectively and the values of $\Delta F/F_0$ in the center one. The considered cleft has a total number of 10 RyRs, a radius of 185.9 nm and the spark a FDHM of 7.2 ms.